YILDIRIM BEYAZIT UNIVERSITY

GRADUATE SCHOOL OF NATURAL AND APPLIED SCIENCES

THE EFFECTS OF THE DC BIAS LINES ON TERAHERTZ PHOTOMIXER ANTENNAS

MSc Thesis by

Adem YILMAZ

Electronics and Communication Engineering

August, 2015

ANKARA

THE EFFECTS OF THE DC BIAS LINES ON TERAHERTZ PHOTOMIXER ANTENNAS

A Thesis Submitted to the

Graduate School of Natural and Applied Sciences of Yıldırım Beyazıt University

In Partial Fulfillment of the Requirements for the Degree of Master of Science in Electronics and Communication Engineering, Department of Electronics and Communication Engineering

by

Adem YILMAZ

August, 2015

ANKARA

M.Sc THESIS EXAMINATION RESULT FORM

We have read the thesis entitled **"THE EFFECTS OF THE DC BIAS LINE ON TERAHERTZ PHOTOMIXER ANTENNAS"** completed by ADEM YILMAZ under supervision of Assist. Prof. Dr. Mehmet ÜNLÜ and we certify that in our opinion it is fully adequate, in scope and in quality, as a thesis for the degree of Master of Science.

.....

Assist. Prof. Dr. Mehmet ÜNLÜ

Supervisor

.....

Assoc. Prof. Dr. Asaf Behzat ŞAHİN

(Jury Member)

.....

Assoc. Prof. Dr. Ahmet Fazıl YAĞLI

(Jury Member)

.....

Prof. Dr. Fatih V. ÇELEBİ

Director

Graduate School of Natural and Applied Sciences

ACKNOWLEDGEMENTS

I would like to express my sincere gratitude to my thesis supervisor Assist. Prof. Dr. Mehmet ÜNLÜ, for his guidance, generous support, and encouragement.

I also thank my family for their endless love, advice and encouragements.

CONTENTS

LIST OF TABLES

LIST OF FIGURES

THE EFFECTS OF THE DC BIAS LINES

ON TERAHERTZ PHOTOMIXER ANTENNAS

ABSTRACT

Photomixer antenna is an essential part of photomixer design. The development on photomixer antennas has still being received considerable attention. DC bias lines are being used in photomixer design to provide required DC voltage to photomixer antenna in order to collect the electron-hole pairs that is excited by a laser beam focused on semiconductor substrate.

This research investigates the effects of the DC bias lines on several types of antennas for terahertz photomixers and proposes a method, namely resistively loaded lines (RLL), to compensate the effects of the DC bias lines. The RLL is formed by placing lumped resistances periodically on the DC bias line in order to cease the leakage current virtually, which cause a significant amount of distortion on the antenna performance. In order to achieve a proper simulations of bias line effects on photomixer antennas, a parametric investigation is carried on electromagnetic simulator HFSS to obtain an optimized simulation technique. The simulation results of the dipole, folded dipole, log-periodic, and spiral antennas show that RLL almost removes the effects of the bias lines and improves the radiation pattern notably compared to that of the commonly used bias line types, such as coplanar stripline and photonic bandgap type bias lines.

Keywords : terahertz, photomixer, antenna, DC bias line, numerical method

TERAHERTZ FOTO KARIŞTIRICI ANTENLER ÜZERİNDEKİ DC BAYAS ŞERİTHAT ETKİLERİ

ÖZET

Foto-karıştırıcı düzeneklerinde antenler çok önemli bir yer tutar. Bu antenlerin geliştirilmesi üzerine çalışmalar artarak devam etmektedir. Doğru Akım (DC) bayas şerithatlar gerekli DC gerilimini antenlere taşıyabilmek için foto-karıştırıcı düzeneklerinde yer alırlar. Foto-karıştırıcı antene uygulanan DC gerilim, bir sürekli dalga aracılığıyla yarı-iletken malzemeler üzerinde uyarılan elektron-hole çiftlerinin toplanıp bir akım dolaşımı oluşturulabilmesi için gereklidir.

Bu araştırmada, DC bayas şerithatların farklı terahertz foto-karıştırıcı antenler üzerinde oluşturduğu etkiler incelenmiştir. Bu doğrultuda, DC bayas şerithat etkisini minimum düzeye indirgeyebilmek için yeni bir metot önerilmiştir. Önerilen bu metotta, empedans yüklü şerithat (RLL), eşdüzlemsel şerithattı belli periyotlara bölerek, bölünmüş parçalar arasına empedans yerleştirilmesiyle oluşturulmuştur. Böylelikle, bayas şerithat üzerine sızabilecek terahertz akımın engellenmesi amaçlanmış ve DC bayas şerithatların anten performansı üzerindeki etkisinin minimuma indirgenmesi öngörülmüştür. Bu etkileri uygun simülasyon koşullarında inceleyebilmek için, kullanılan HFSS programı üzerinde parametrik bir çalışma yapılmış olup optimum simülasyon prosedürü elde edilmiştir. Bu prosedür ile yapılmış olan bayas şerithatlı anten simülasyonlarda, önerilen RLL'in dipol, katlanmış dipol, spiral ve log-periyodik antenler üzerindeki DC bayas şerithat etkisini kaldırdığı ve anten performansının eklenen bayas şerithatlardan etkilenmediği gözlemlenmiştir. Ayrıca, literatürde yaygın olarak kullanıldığı gözlenen eş-düzlemsel şerithat ve fotonik bant tipi bayas şerithatlarla karşılaştırma yapıldığında, RLL'in anten ışıma örüntüsünü bozmadığı görülmüştür.

Anahtar kelimeler: terahertz, foto karıştırıcı anten, DC bayas şerithat, sayısal metot

CHAPTER 1

INTRODUCTION

1.1. THz Technology

Terahertz (THz) waves refer to electromagnetic radiation that has a frequency between 0.3 THz and 10 THz, occupying a large portion of the electromagnetic spectrum between microwave and infrared bands [1]. THz band, which has variously been named such as sub-millimeter, far infrared and near millimeter wave, is depicted in Figure 1.1. Even though this part of the electromagnetic spectrum remains the least explored region mainly due to the technological challenges of producing efficient and compact sources/detectors suitable for THz radiation, it offers some unique properties when compared to its neighbor ranges, microwave-millimeter and infrared areas. Some of these properties can be listed as follows:

- *Penetration:* The THz radiation has relatively longer wavelength than the infrared ones; which enables THz wave to penetrate many materials such as paper, soil, fabric, plastic and wood. Therefore it can be used in security to detect the threat objects inside luggage, mail, and especially on people since using THz waves of a few meV of photonic energy is much safer than using X-rays [2].

- *Resolution:* THz waves have shorter wavelengths in comparison to the microwave ones; hence a better spatial imaging resolution can be achieved by THz waves.

- *Safety:* THz radiation is non-ionizing. The photon energies in THz band are much lower when compared to X-rays. Therefore it is not expected to damage tissues and DNA, unlike X-rays, which makes them much safer in medical

imaging. Diagnosing and imaging some cancer tissues can be given as an example [3]. Another important feature of THz waves used in biotechnology for sensing chemical and biochemical compounds is that biological structures including DNA exhibit characteristic motions such as, rotation, vibration or twisting at THz frequencies. It is possible to detect the presence of mutation in a DNA sequence using THz [4].

- *Spectral fingerprint:* Many materials show their own absorption and reflection features in the THz range, therefore distinguishing the different ingredients and materials is easier in the THz range of the electromagnetic spectrum [5].

- *Large bandwidth:* In communication systems, THz frequency provides a very large bandwidth; hence it enables the transmission of broadband signals and carrying large amount of information. Also, the size of antenna and its equipment will be reduced at THz frequencies. Due to the water vapor in atmosphere, free space communication is limited to short a distance which is suitable for short distance wireless communications and networking very promising for future communication systems with faster speeds than current UWB (Ultra-wideband) technology [6]. On the other hand at high altitudes, THz wave transmission is almost lossless and makes aircraft-satellite or satellite-satellite communication possible.

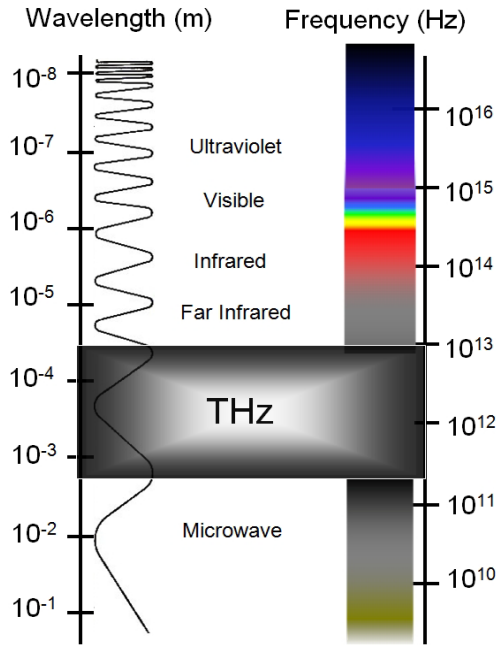

Figure 1.1 Schematic diagram of electromagnetic spectrum.

1.2. Motivation and Objective

Terahertz technology has been recently receiving considerable attention due to its potential applications on a variety of fields such as medical imaging, wireless communication, security, material spectroscopy, and pharmaceutical [7 - 12]. Although a great deal of effort has been spent on developing several different components for terahertz systems, the main concentration is focused on the terahertz sources and detectors [13 - 19], the development of which is still the most important challenge in this field. Photomixing is one of the most commonly used techniques for continuous-wave (CW) terahertz generation or detection [20 - 28]. Photomixing, also known as optical heterodyne conversion, is a method of generating CW THz radiation in which two laser beams that have close frequencies or a dual mode laser excite an active semiconductor area. The advantage of this technique is the wide tunability of the output THz frequency which is determined by the frequency difference of two CW laser beams. On the other hand, a low optical-to-THz conversion efficiency, which is defined

by ratio of the THz output power to the input optical power, is the main drawbacks of this technique [29, 30]. In a photomixer device, an integrated planar antenna, which is so called photomixer antenna, is used in order to radiate the excited THz wave to the free space. The integrated THz photomixer antenna devices are one of the best developed parts of photomixers. The most commonly used photomixer planar antennas that exist in literature are dipole [15, 20, 27, 31, 32, 40, 41], folded dipole [33 - 35], log periodic [36 - 38, 40], bow-tie [27, 28, 38], and spiral antennas [21, 28, 38 - 41]. Each of planar antennas is chosen in a photomixer design to take the advantages of their own characteristic properties such as existing high impedance or offering impedance over wide range of bandwidth.

The basic working principle of a typical CW THz photomixer device is shown in Figure 1.2, where a dipole antenna is used as an example of photomixer antenna. As it can be seen from figure, the optical excitation is directed on photoconductive gap, which is the gap between the arms of dipole antenna. The laser beams illuminate the device on the photoconductive gap and generates the electron and hole carriers in this area. In order to collect the excited carriers, a DC voltage is needed. This voltage is carried by using the DC bias lines that are connected to the antenna terminals. By following this way, the generated THz photo-current acts as the exciting source at the antenna feed point and the coupled antenna will radiate the THz wave into the free space. Figure 1.3 shows the equivalent model of the THz photomixer antennas, where I is the current drawn from the bias source, V_{bias}. Capacitance between electrodes is represented as C, and antenna is represented as R_a.

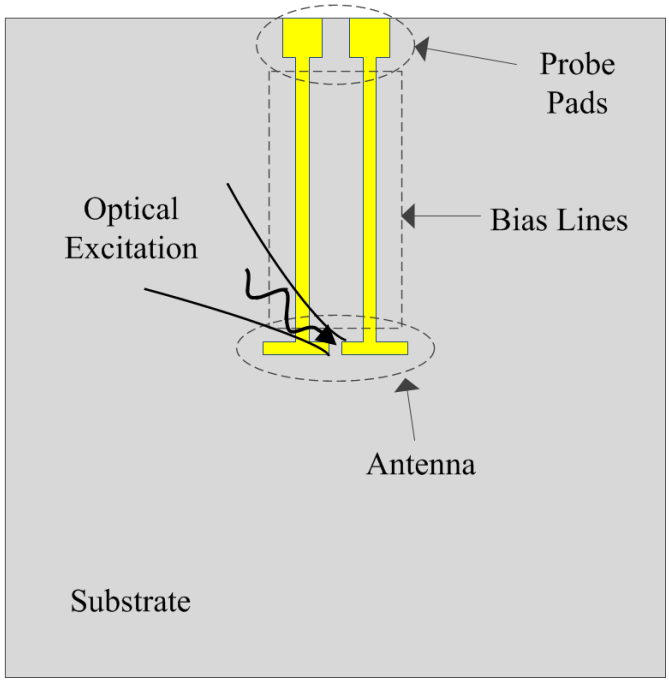

a) The layout of a generic photomixer antenna

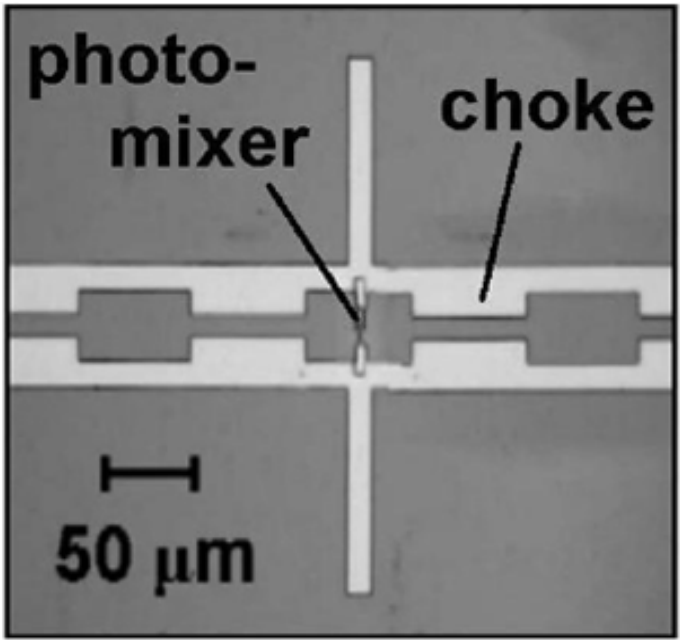

b) The photograph of an example photomixer antenna [41]

Figure 1.2 (a) to **(b)** Photomixer antenna.

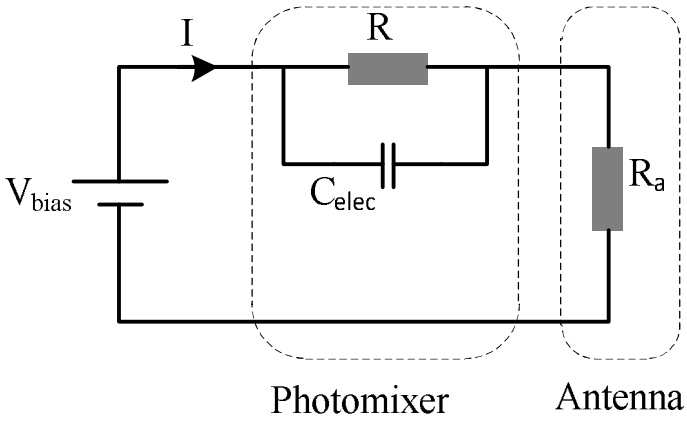

Figure 1.3 Equivalent circuit model of photomixer antenna.

The main goal of this thesis is to study the effects of these DC bias lines on radiation characteristics of the antenna from the electromagnetic radiation perspective. The effects of DC bias lines are mostly neglected although they have a significant effect on the radiation performance of the photomixer antenna. The bias line dimensions that are being used by the community are generally much larger when compared to the dimensions of the antenna itself [40, 43 - 50] which will directly effects the radiation performance of the photomixer antenna. Therefore, reducing the DC bias line effects still remains under investigation and different kind of DC bias lines are suggested for this purpose.

One of the most popular, and easy to design, bias line type is coplanar stripline (CPS) [41, 43, 45, 46, 59]. They are basically composed of two thin metal lines which actually behave as a high impedance transmission line between the DC supply and photomixer antenna. The dimensions of CPS are most of the time comparatively larger than the antenna; in addition to that, they are directly connected to the antenna itself, which results in a considerable amount of current leakage to the CPS, causing a significant distortion on the radiation pattern and input impedance, and a considerable loss of generated or detected power.

A better alternative for bias lines is using photonic bandgap type structures [40, 41, 44 - 47, 49, 50]. Photonic bandgap structures (PBG) are designed as filters that are formed using high and low impedance sections through CPS. The PBG bias lines are also connected directly to the photomixer antenna just as the CPS bias lines, the current leakage from the antenna can be reduced to a certain extent by a proper design; however, they still cause an important malformation on the current distribution, and hence, the radiation pattern of the antenna is distorted drastically. Moreover, the radiated power decreases due to the leakage current running on the long bias lines. As a result, these two types of bias lines affect the antenna radiation pattern and input impedance notably, they decrease the antenna efficiency; hence, a better solution is needed.

In this thesis, a new type of bias line, namely resistively loaded line (RLL), is studied for the biasing of the photomixer antennas, where the conventional CPS bias line is delimited by a set of periodically placed lumped resistances. The lumped resistances are formed using a resistive thin film that has a high and adjustable resistivity, such as silicon chromium (SiCr) or tantalum nitride (TaN), which makes it possible to adjust the resistance level specifically for each design. Different types of photomixer antennas with the CPS, PBG, and RLL bias lines have been designed in order to compare the effects of all three types of bias lines.

1.3. Thesis Overview

This research is organized as follows. A brief review of THz technology and CW THz photomixer sources with particular emphasis on photomixing theory and concept as well as important factors such as antenna and bias lines in the photomixer performance are presented in Chapter 1.

Chapter 2 will discuss a computational simulation method, such as High Frequency Structure Simulator (HFSS), to achieve a best result when simulating such a photomixer

antenna. The effects of airbox size, port meshing, boundary condition, and choosing the proper size of a substrate will be discussed.

In Chapter 3, the characterization of bias lines will be given. Design parameters for each of bias lines will be given. Then, the bias lines will be treated as two port networks and the numerical studies will be carried out. Since the two-port network results of bias lines indicates the isolation between DC bias pads and antenna, the possible effects of each bias line on photomixer antennas will be discussed.

In Chapter 4, the design parameters of antennas that will be used for testing structures of bias lines will be discussed, and then different kind of planar antennas will be designed. The performance of antennas with each bias line will be compared in a perspective of radiation pattern and input impedance of antenna.

Finally, Chapter 5 concludes this research and suggests the future directions.

CHAPTER 2

NUMERICAL METHOD

2.1. Finite Element Method (FEM) and High Frequency Structure Simulator (HFSS)

Finite Element Method (FEM) is a very powerful numerical technique that is used for solving complex engineering problems. In this method, a complex structure is divided into smaller sections of finite dimensions known as elements. These elements are connected to each other via joints called nodes. These processes can be seen in Figure 2.1, where actual size of the structures is divided into much smaller elements (also called as mesh) to obtain a solution rather easily. The solution is started with each unique element independently, which drastically reduces the solution complexity. The final solution is then computed by reconnecting all the elements and combining their solution. These processes are named assembly and solution respectively in FEM [51].

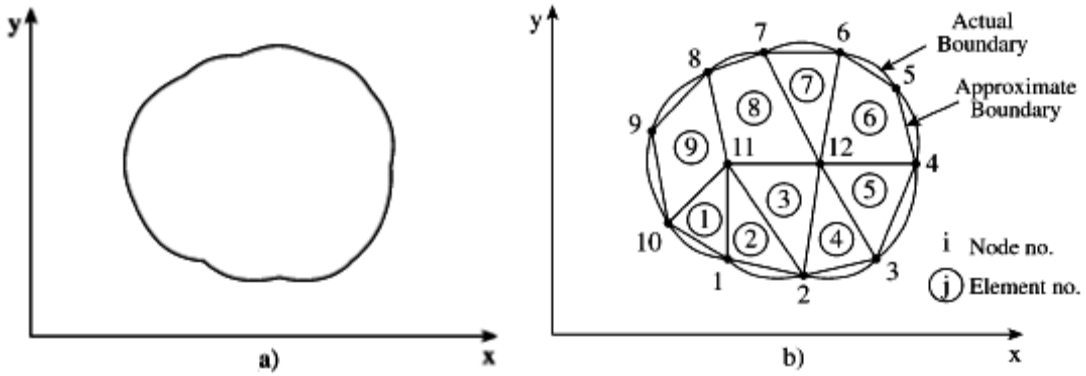

Figure 2.1 Discretization process of FEM (a) the solution region (b) finite element discretization [52].

High Frequency Structure Simulator (HFSS) is a three-dimensional (3-D) full-wave electromagnetic simulator that implements FEM [53]. In this thesis, HFSS is mainly used as a design tool for structures and numerical simulation of them. There are some

main steps that need to be understood for a simulation in HFSS: structure modeling, excitation of structure, defining boundary condition, setting up solution parameters and getting post-processing results.

In HFSS, modeling a structure, which can be created in 2-D, 3-D or combination of them, is relatively easy. HFSS offers objects to be drawn either directly or equation based, which gives flexibility to users in modeling structures. HFSS offers an extensive library for material assignment. Also, it is possible to create new materials not contained in the library of HFSS. In this thesis, substrates are modeled as three dimensional Gallium Arsenide (GaAs) objects, and the radiators and feedings of designed antennas with bias lines are modeled as two dimensional, which are defined as perfect electric boundary in order to see the effects of bias lines on antenna efficiency more clearly. The designed three dimensional models that will be tested structure for various HFSS parameter in this section is shown in Figure 2.2.

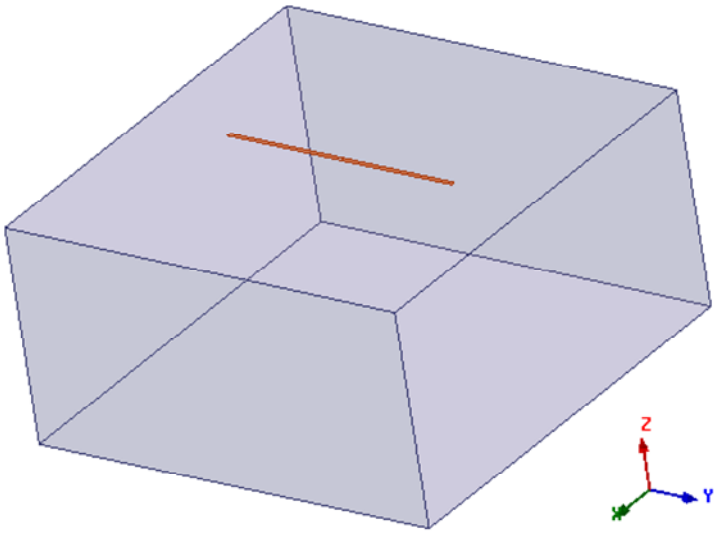

Figure 2.2 Designed dipole antenna in HFSS.

In order to excite the designed structures, HFSS offers many types of excitation such as wave port, lumped port, terminal, and floquet port. The first two types are mainly used throughout this thesis. Wave ports take place in a design internally or externally. On the

other hand, lumped ports are recommended only for surfaces internal to the geometric model, and S-parameters can be directly calculated at ports.

The modeled structures need to be specified by boundary conditions. There are two main options in HFSS: radiation boundary and perfectly matched layer (PML). The radiation boundary (or Absorbing Boundary Condition, ABC) allows waves to radiate infinitely far into space. The boundary is normally assigned to an airbox, which is placed away from any radiating object at least one quarter wavelength of minimum operating frequency. A drawback to this boundary is that if there is any energy incident at an angle greater than 30 degrees it will be reflected. As in the radiation boundary, the PML also allows waves to radiate infinitely far into space. The PML is not strictly a boundary condition but a fictitious material that fully absorbs the electromagnetic fields impinging upon the PML boundary. The main advantages of the PML is that there is no angle of incidence problem and the boundary can be placed away from any radiating object at least one tenth of a wavelength of minimum operating frequency. These two boundary conditions are applied to the structures during this thesis work. Figure 2.3 shows the designed structure enclosed in an airbox with and without PML boundary.

The next step of the simulation process is to specify solution parameters such as solution (adaptive) frequency, maximum number of passes and maximum delta S parameters. In HFSS, adaptive frequency is usually set to expected solution frequency or about solution frequency. After selecting the adaptive frequency, the frequency sweep is defined in order to perform an adaptive analysis in a range of frequencies. While specifying the frequency sweep, there will be three options to be selected: discrete, interpolative, and fast sweep. Discrete sweep performs a full solution at every frequency specified in the sweep, hence offers the highest accuracy. This sweep is best when only a few frequency points are necessary to accurately represent the results in a frequency range. Interpolative sweep estimates a solution for an entire frequency range. This sweep is best when the frequency range is wide and the frequency response is

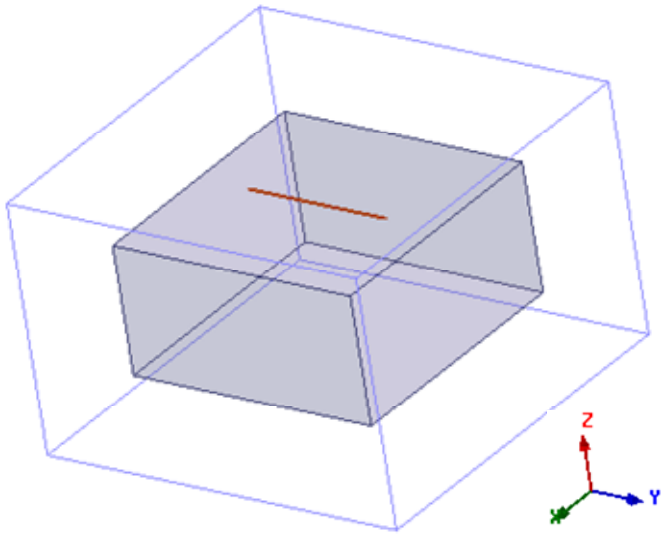

a) Airbox without boundary

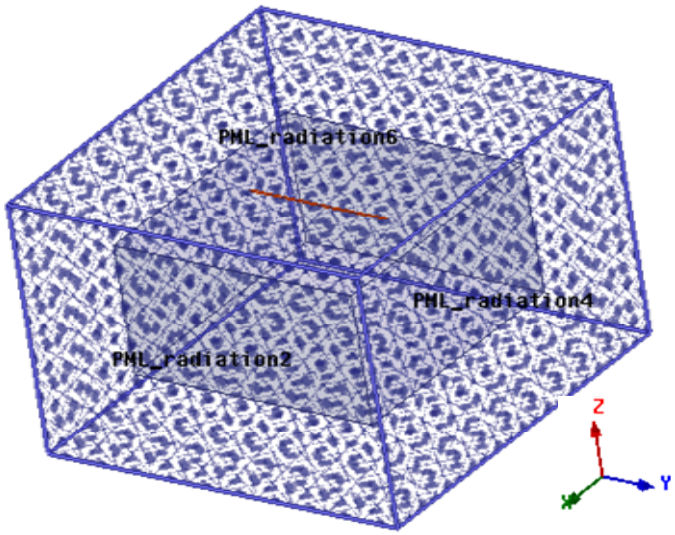

b) Airbox with boundary

Figure 2.3 (a) to **(b)** HFSS model with and without PML boundary.

smooth. Fast sweep generates a unique full-field solution for each division within a frequency range. This sweep is best for models that will abruptly resonate or change operation in the frequency band. A fast sweep will obtain an accurate representation of

the behavior near the resonance. Either the discrete or fast sweep is used throughout this thesis.

During the simulation process of designed model, HFSS refines the mesh in an ordered cycle; hence it is important to specify convergence of the solution, which is named as maximum delta S in HFSS. The mesh refinement stops when it reaches a specified maximum delta S, which is normally 2% or less. In addition, it is important to specify at least two consecutive convergent passes for higher accuracy. In Figure 2.4, a solution data with 0.01 max delta S and 4 consecutive convergent in a HFSS is shown. During simulations, one should keep in mind that, convergence criteria directly effects solution time and amount of the required memory. In this thesis, two consecutive converged passes within the specified maximum delta of 0.02 or 0.01 are interested.

Final step of simulation process in HFSS is getting post-processing results. When a solution is completed, convergence information, mesh statistics, S-parameters, impedances and radiation parameters can easily be viewed and plotted.

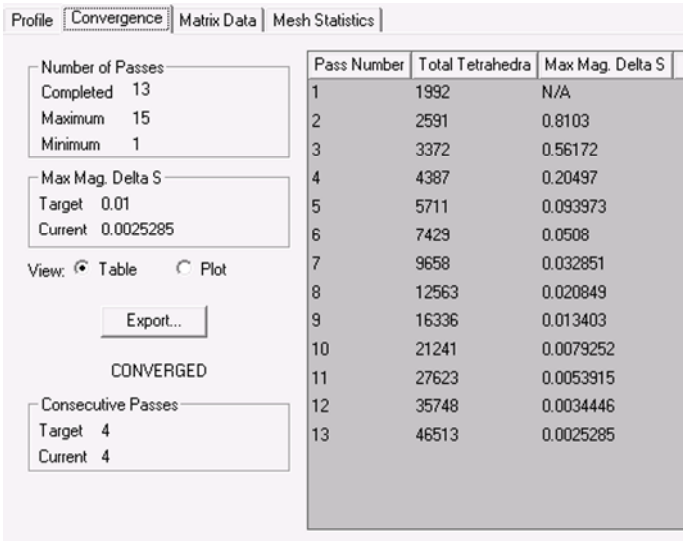

Figure 2.4 Solution data for thirteen passes view in HFSS.

In order to investigate the effects of aforementioned major parameters in HFSS, a series of simulation is run with the designed dipole antenna. The design parameters of dipole antenna are as follow: it has a dipole length of 230 μm, which is placed on a Gallium arsenide (GaAs) substrate of lateral dimensions 400 μm and thickness 200 μm. It is important to note that the outcomes of this chapter constitute the basis of all simulation during this thesis.

2.2. Variation of Solution Parameters

Specifying the solution parameters in HFSS defines the accuracy of simulation. For this reason, various simulations are run with designed dipole antenna to investigate the effects of these parameters. General simulation conditions for dipole antenna are as follows: substrate and antenna arms are assigned as Gallium arsenide (GaAs) and perfect electric conductor (PEC), respectively. PML is applied as boundary condition, and a frequency sweep between 350-400 GHz is specified. For each trial run, certain parameters such as max delta S, solution frequency and total number of mesh are being altered in these simulations. As the impedance of photomixer antennas is essential in this thesis, results of maximum real impedance and frequency where it exits are considered mostly. The details and results of simulations are shown in Table 2.1.

First solution parameter that is being under investigation is max delta S. Two different values of this parameter are chosen for convergence criterion of first simulation. It can be deduced from Table 2.1 that with a smaller max delta S, total number of mesh is increased; hence simulation time and system memory usage is consequently increased. It is also important in a simulation that convergence should be satisfied at least two consecutive max delta S convergent. By doing so, the probability of miscalculation due to mesh refinement on structure will be prevented; hence accuracy of convergence will be guaranteed. For this reason, the designed antenna is also simulated with 2, 3, and 4 consecutive convergent criteria, which increases simulation time as expected. Although, first two consecutive convergent are enough for an accurate simulation, 4 consecutive

convergent is also applied to solve the structure with greater mesh number, hence investigate the simulation results when they are solved with greater mesh.

As HFSS offers different frequency sweep over solution frequency band, two of them, namely as fast and discrete sweeps, are applied to designed structure in order to compare these two simulation sweep methods. The simulation results are illustrated in Figure 2.5, where one can say that these two sweeps give the exactly identical results for a structure simulation. In addition, results in Table 2.1 indicate that the discrete-sweep simulation has longer simulation run time than the fast-sweep simulation. This is mainly because the solution in discrete-sweep occurs at each frequency point separately.

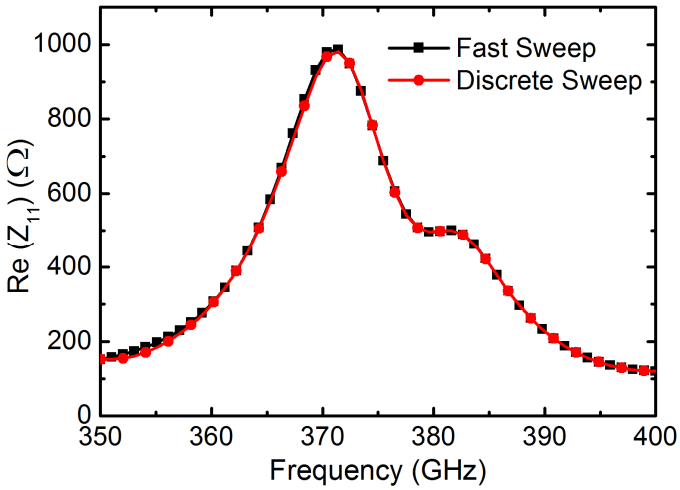

Figure 2.5 Fast and discrete sweep solution results.

Mesh refinement in HFSS also depends on solution frequency of structure. Specifying different solution frequency produces different mesh refinement. Although it is suggested to define the solution frequency at around resonance frequency, various solution frequencies are applied to designed structure in order to see their effect on mesh refinement. The details for these simulations are listed in Table 2.2.

Table 2.1 HFSS solution parameters: variation of max delta S and total mesh number.

Simulation Parameters			**Simulation Data**			
Simulation	**Max Delta S**	**Consecutive Convergence**	**Tetrahedral in Mesh**	**Passes before Convergence**	**Run time (min.)**	**Real max(Z_{11}) (Frequency)**
1 - Fast	0.02	1	16336	9	3.5	995.3 (369.69 GHz)
1 - Discrete					9	979 (369.3 GHz)
2 - Fast	0.01	1	21241	10	5	991 (370.20 GHz)
2 - Discrete					10	981 (370.41 GHz)
3 - Fast	0.01	2	27623	11	5.25	989 (370.70 GHz)
3 - Discrete					16.25	977 (370.41 GHz)
4 - Fast	0.01	3	35748	12	8	989 (370.70 GHz)
4 - Discrete					20.45	979 (371.43 GHz)
5 - Fast	0.01	4	46513	13	9	986.2 (371.42 GHz)
5 - Discrete					25	981 (371.43 GHz)

Table 2.2 HFSS solution parameter: variation of solution frequency.

Simulation Parameters			**Simulation Data**		
Simulation	**Max Delta S**	**Solution Frequency (GHz)**	**Tetrahedral in Mesh**	**Run time (min.)**	**Real max(Z_{11}) (Frequency)**
1 - Fast	0.01	360	27517	5.45	981.9 (370.85 GHz)
2 - Fast	0.01	370	46513	10.5	989 (371.11 GHz)
3 - Fast	0.01	375	36121	7.5	983.9 (371.11 GHz)
4 - Fast	0.01	380	27443	7	981.2 (370.85 GHz)

When comparing the real impedances for two sweep methods illustrated in Table 2.1, it can be seen that the results are slightly different. This difference occurs due to the defined number of steps over solution frequency band. In order to obtain the most accurate results for real impedances and where they exists, number of steps over frequency band are increased for both sweep method. The details and results of these simulations are shown in Table 2.3.

Table 2.3 HFSS solution parameters: variation of steps over frequency sweep.

Simulation Parameters			**Simulation Data**	
Simulation	**Max Delta S**	**Number of Steps**	**Run time (min.)**	**Real max (Z_{11}) (Frequency)**
1 - Fast	0.01	50	8.5	986 (371.42 GHz)
1 - Discrete	0.01	50	24.5	981 (371.42 GHz)
2 - Fast	0.01	100	9	988 (371.21 GHz)
2 - Discrete	0.01	100	41	981 (371.21 GHz)
3 - Fast	0.01	150	9.5	989 (371.14 GHz)
3 - Discrete	0.01	150	50	981 (371.14 GHz)
4 - Fast	0.01	200	10	989 (371.10 GHz)
4 - Discrete	0.01	200	85	981 (371.10 GHz)

In brief, it is important for an accurate simulation in HFSS to define the solution parameters correctly. There should be at least two consecutive convergent with 0.01 max delta S parameter for most accurate results. Also, the larger mesh defines the precision of simulation but it will give increased simulation time and system memory usage. In addition, there is no significant difference between discrete and fast sweep

methods except the simulation run time. When the accuracy of simulation is critical, more steps over frequency band can be defined with considering the time consumption. As a result, once the fundamental conditions are satisfied, it is a trade-off between more accuracy results and simulation time.

2.3. Variation of Boundary Conditions

As mentioned in Section 2.1., there are some restrictions in covering the structure with airbox. In order to clarify effects of airbox size that is assigned as Perfectly Matched Layer (PML) and Absorbing Boundary Condition (ABC), a fast sweep design with 0.01 delta max S is simulated with varying airbox size. In these simulations, the solution frequency is specified as 370 GHz, and fast frequency sweep is defined between 350 to 400 GHz with 150 steps over frequency band. In Figure 2.6, the effects of airbox variations with PML and ABC boundary conditions are illustrated. Note that in these figures, letters of A, B, and C refers to airbox size of 550*350 μm, 800*600 μm, and 1000*800 μm, respectively. It can be seen from figures that variation of PML airbox size does not significantly affect results. On the other hand, airbox size of ABC has important effect on results, especially when it is closer to simulated substrate. This mainly occurs due to the reflected energy back into the substrate.

In order to obtain a comparison between PML and ABC boundary conditions, a fast sweep design with 0.01 delta max S is simulated with two boundary conditions. The results are illustrated in Figure 2.7, where one can see that two boundary conditions have almost same effect on results.

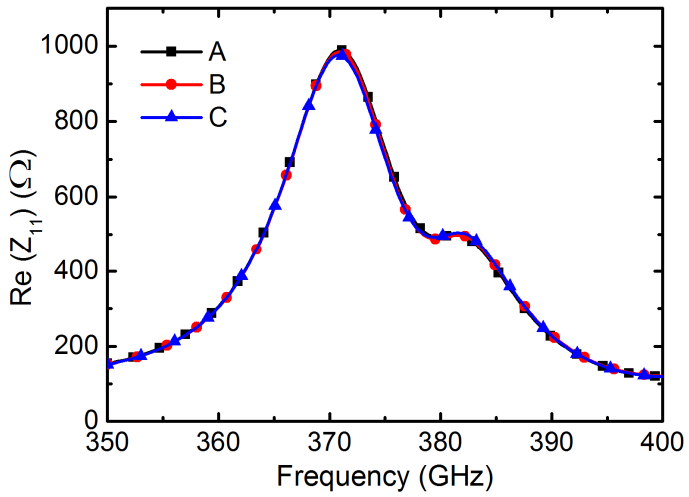

a) Airbox assigned as perfectly matched layer (PML)

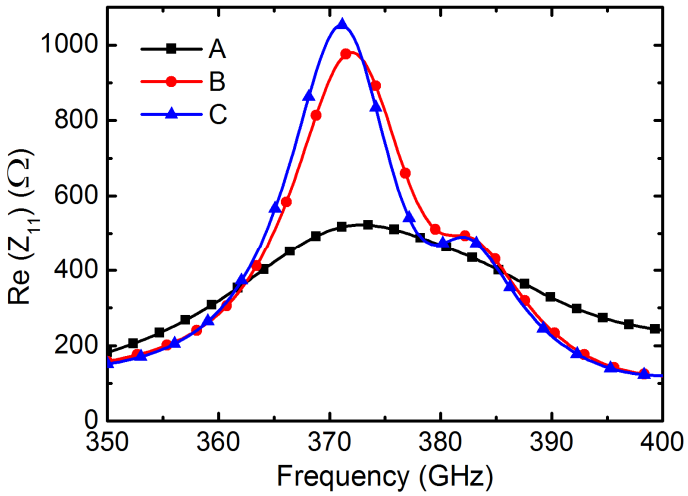

b) Airbox assigned as absorbing boundary condition

Figure 2.6 (a) to **(b)** The effects of airbox size variations.

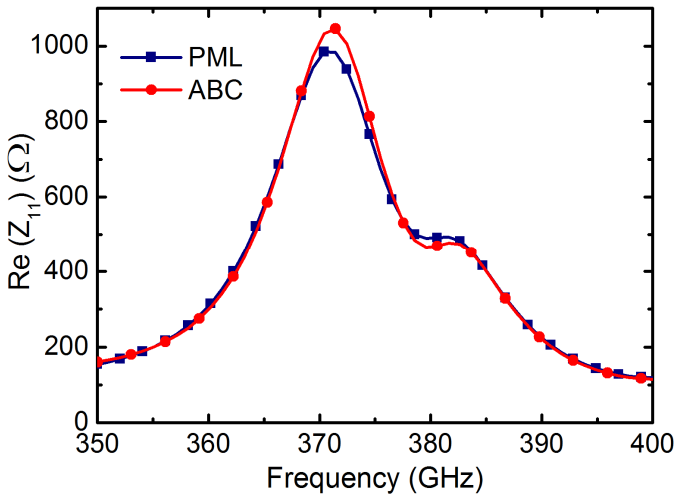

Figure 2.7 PML and ABC solution results.

As a conclusion, the important parameters for an accurate simulation in HFSS are investigated in this chapter. Once the structure is modeled and excitation of structure is decided, defining boundary condition and setting up solution parameters must be carefully chosen in order to obtain accurate results. The outcomes of this chapter are utilized during the numerical studies of bias lines and antennas in following chapters.

CHAPTER 3

DESIGN OF BIAS LINES

In this chapter, the bias lines are first analytically designed using closed form equations, and then simulated using a full-wave electromagnetic solver, HFSS. The behavior of each bias line is investigated as a two port network, and their possible effects on photomixer antennas are discussed through this chapter.

3.1. Bias Line Types

The requirement of bias lines in a photomixer design arises from necessity of collecting the excited electron-hole pairs from photoconductive gap area by providing DC voltage to the photomixer antenna. For this purpose, different types of bias lines are employed in literature in order to carry the required DC voltage to the photomixer antenna [30, 41, 43 - 46, 48]. The diversity of bias lines is originating from blocking the THz current into the bias lines and hence reducing the possible effects of them on antenna performance. One of the popular, and easy to design, bias line is coplanar striplines (CPS). The CPS takes places in a photomixer design as a direct connection between the probe pads and antenna. Although CPS can be designed easily in photomixer antennas, it fails to be successful at blocking the THz current, and hence distorts the antenna performance significantly. For this reason, there has been conducting researches on improvements of CPS in order to minimize the bias line effects on antenna performance. The Photonic Band Gap (PBG) type of bias line can be shown as an example to that kind of advanced bias line. The PBG structure is an array of metallic periodic pattern placed along the coplanar striplines. The low impedance and high impedance surfaces are constituted by added metallic surface throughout the CPS and the bias line acts as a filter with these advancements in photomixer design. Therefore, the PBG type bias line shows ability to

mitigate THz current through the line and enhances the reducing of the current leakage into lines when compared to the CPS.

In this thesis, Resistively Loaded Line (RLL) type of bias line is proposed for photomixer antennas. In this case, the conventional CPS bias line is delimited by a set of periodically placed lumped resistances. The lumped resistances are formed using a resistive thin film that has a high and adjustable resistivity, such as silicon chromium (SiCr) or tantalum nitride (TaN), which makes it possible to adjust the resistance level specifically for each antenna design. By achieving a proper design of RLL, current leakage into bias line will reduce to minimum, and antenna performance will be barely affected.

In order to clarify the working principle of each aforementioned bias line, they are first analytically designed using closed form equation, and then they are treated as two-port networks. The simulation results of bias lines are examined first; the advantages and disadvantages of each bias line are outlined in this chapter.

3.1.1 Coplanar Stripline (CPS) Type of Bias Line

Coplanar striplines have been extensively studied and characterized. The design variables for a symmetric CPS are the gap between the strips, *d*, and the width of the strips, *a*, as shown in Figure 3.1-(a). Also, the equivalent circuit for CPS is given in Figure 3.1-(b). In order to obtain the impedance of a symmetric CPS on a substrate of thickness *h*, calculation steps can be given as follows [54];

$$k = \frac{d}{2a + d} \tag{3.1}$$

$$k' = \sqrt{1 - k^2} \tag{3.2}$$

$$k_1 = \frac{\sinh\left(\frac{\pi d}{4h}\right)}{\sinh\left(\frac{\pi(2a+d)}{4h}\right)} \tag{3.3}$$

$$k_1' = \sqrt{1-k_1^2} \tag{3.4}$$

$$\varepsilon_{eff} = 1 + \frac{\varepsilon_r - 1}{2}\frac{K(k')}{K(k)}\frac{K(k_1)}{K(k_1')} \tag{3.5}$$

$$Z_0 = \frac{\eta_0}{\sqrt{\varepsilon_{eff}}}\frac{K(k)}{K(k')} \tag{3.6}$$

where $\eta_0 = \sqrt{\mu_0 / \varepsilon_0}$, ε_r is the relative dielectric constant of the substrate, K is the complete elliptical integral of the first kind.

In order to clarify the behavior of CPS bias line, one of the CPS design, which has a gap of 36 μm and strip width of 2 μm, is designed. The value of impedance for designed CPS is obtained as 197.8 Ω by using the formulas (3.1) – (3.6). The CPS design is also simulated by HFSS, and the two port simulation results are presented in Figure 3.2. It confirms that the CPS type bias line exhibits a typical transmission line [64] (as illustrated in Figure 3.1-(b)) behavior with a high magnitude of transmission coefficient, $|S_{21}|$, forming a direct path between the probe pads and antenna. In addition to that, when this type of bias lines are directly connected to the antenna without any precautions, it will behave as a part of the antenna and contribute to the radiation because there will be a strong amount of terahertz current leakage on the bias lines.

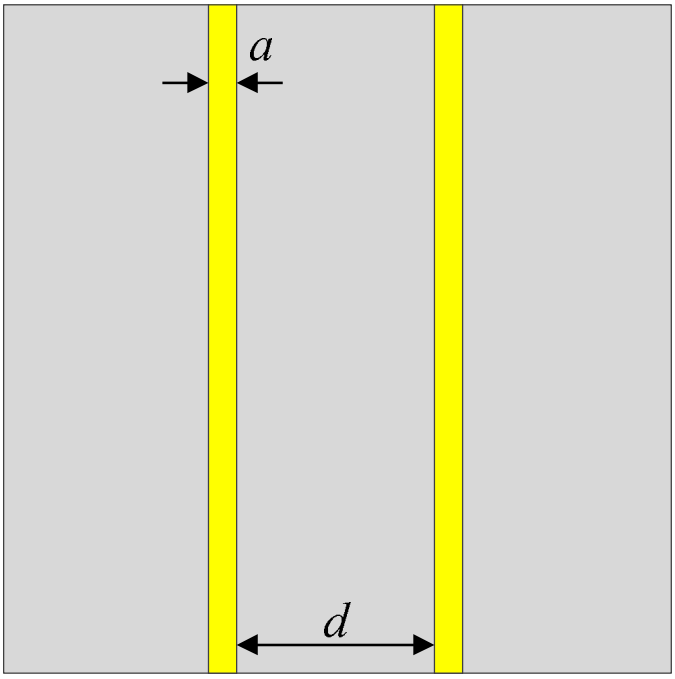

a) Coplanar stripline (CPS) design

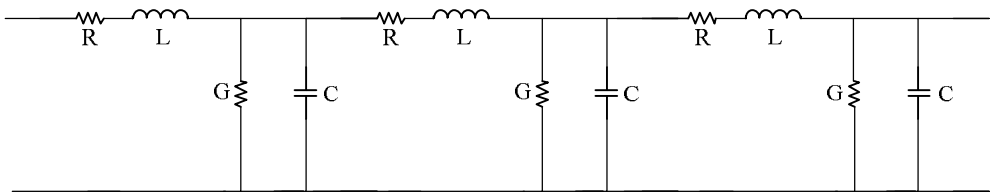

b) Equivalent circuit

Figure 3.1 (**a)** to (**b)** Coplanar stripline (CPS) bias line.

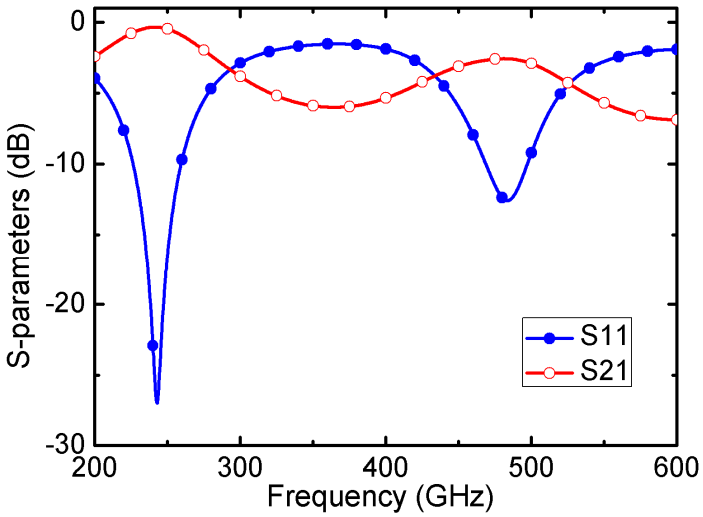

Figure 3.2 Two-port simulation results of CPS

3.1.2 Photonic Band Gap (PBG) Type of Bias Line

The photonic band gap (PBG) bias lines are used as a better alternative to the CPS bias lines, which is shown in Figure 3.3-(a). In THz photomixer designs, the PBG bias line, also called as choke filter, behaves as a filter and reduces the THz leakage into lines. The PBG design is based on CPS discontinuities, which is an addition of metallic load to constitute a high/low impedance sequences through the CPS bias line. These loads bring additional capacitance such as parasitic capacitance, which is due to the proximity of loads, and fringe capacitance, which is due to edge of the loads. The additional effects of inductance and capacitance on a prototype of a low pass filter (Figure 3.3-(b)) are illustrated in Figure 3.3-(c). In this kind of filters, the cut off frequency is specified by lengths of the high/low impedances. As an example performance, a PBG structure with 5 sections of high/low impedances is designed. The design parameters of PBG is as follows; a = 1 μm, b = 70 μm, c = 2 μm, and d = 60 μm. When a 5 sections low pass filter is designed with these parameters, the inductance and capacitance values can be obtained as follows: $L_1 = L_5 = 33$ pH, $L_3 = 69$ pH, $C_2 = C_4 = 0.22$ pF.

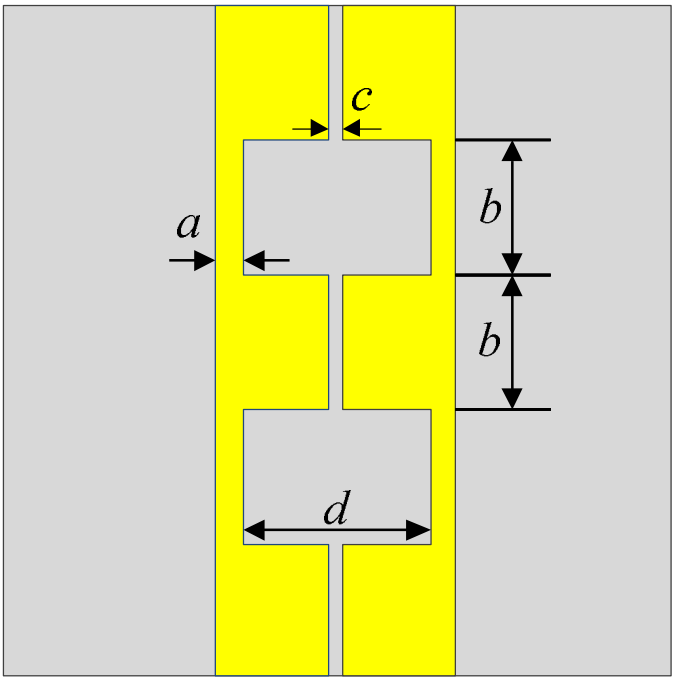

a) Photonic band gap (PBG) design bias line.

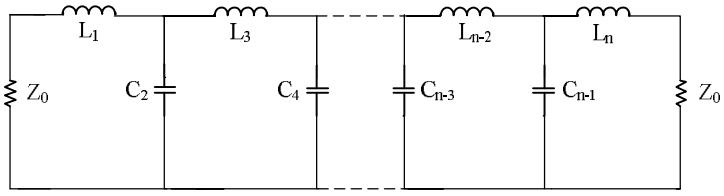

b) Prototype of n section low pass filter

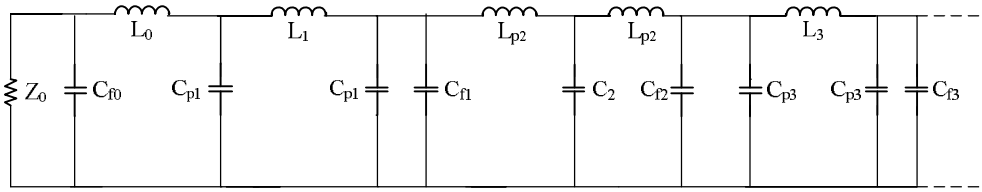

c) Equivalent circuit

Figure 3.3 (a) to **(c)** Photonic band gap (PBG) bias line

The PBG design is simulated with HFSS and results are illustrated Figure 3.4, where one can see that the PBG structure behaves as a low-pass filter with the given dimensions; hence when it is used as a bias line in a photomixer design, it will provide isolation between probe pads and antenna above cut-off frequency. On the other hand,

the PBG bias lines occupy a large metal area, which drastically loads the antenna, and hence contributes to the radiation. Moreover, the PBG bias lines are still not sufficient for wide band applications, since the cut-off frequency of the PBG bias line must be selected at a low frequency, causing the PBG bias line dimensions to grow extensively.

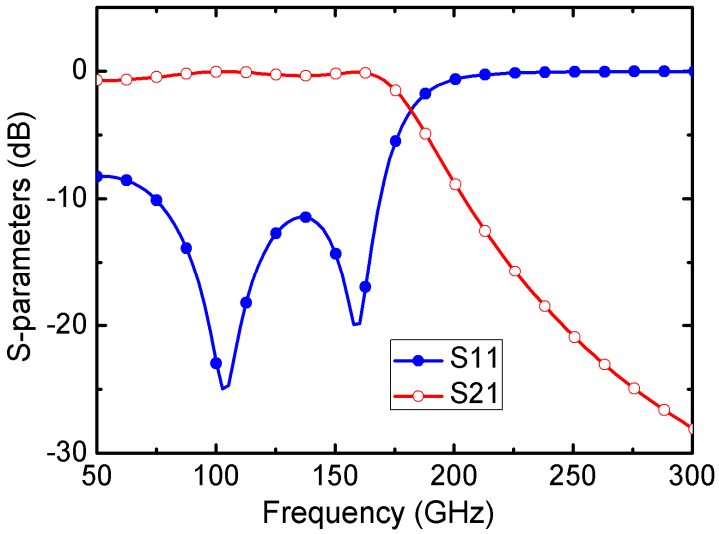

Figure 3.4 Two-port simulation results of PBG bias line.

3.1.3 Resistively Loaded Line (RLL) Type of Bias Line

In CPS and PBG types of bias lines, it is observed that the dimensions of the bias lines are much larger compared to the dimensions of the antenna, which directly causes a considerable distortion on the antenna performance. In addition to that, when CPS and PBG bias lines are directly connected to the antenna without any precaution, they will bring additional losses due to the leakage current towards the bias lines. Therefore, resistively loaded line (RLL) type bias line, which is presented in Figure 3.5-(a), is proposed as an alternative to CPS and PBG. The equivalent circuit of a RLL design is illustrated in Figure 3.5-(b), where one can see that the design is same with CPS except the impedances (R_{RL}) inserted between much smaller striplines. The proposed idea was previously introduced for MEMS reconfigurable antennas working in the microwave

and millimeter-wave frequencies [55 - 57]. The working principle of RLL differs from CPS. In this scenario, the CPS bias line length is divided into much smaller lengths that become much shorter than the wavelength in the band of interest so that they do not load the antenna. The lumped resistors are placed periodically along the divided CPS bias line. The lumped resistances of the RLL lines are implemented as thin-film SiCr or TaN resistors. The conductivity of these layers can be tuned so that the lumped resistance can be easily adjusted in 100 Ω-100 kΩ range.

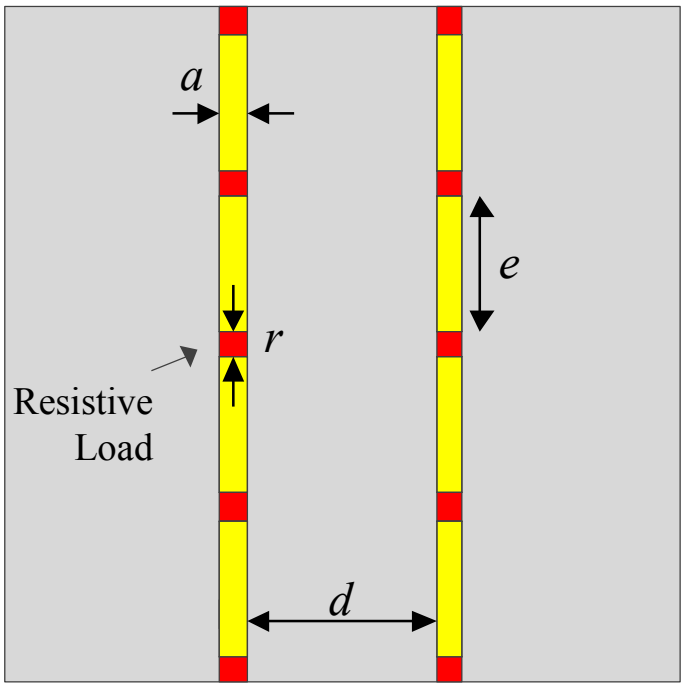

a) Resistively loaded line (RLL) design

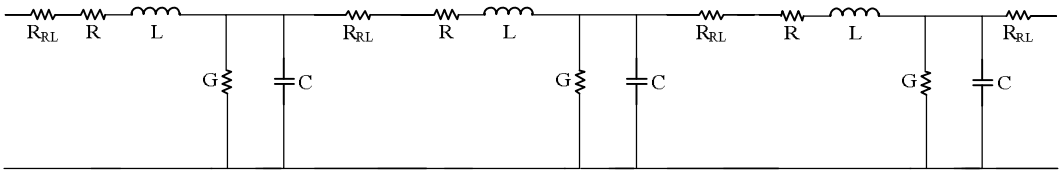

b) Equivalent circuit

Figure 3.5 (a) to **(b)** Resistively loaded line (RLL) bias line.

As an example performance, a RLL design with 1 kΩ resistor is designed and simulated. It is clearly seen from simulation results in Figure 3.6 that the RLL prevents the current leakage on the bias lines and guarantees the isolation between the probe pads and antenna in a wide frequency band. In addition, the value of impedances is varied between 20 Ω to 1 kΩ, and it is seen that the isolation between two ports can be still achieved within these values. Therefore, the distortion on the antenna radiation characteristics will be minimized when the RLL bias lines with are used. Within a proper design of RLL, THz transmission will be reduced while providing a perfect transmission of bias current.

The only drawback of using RLL bias lines for the photomixer antennas is that the applied DC voltage needed for the operation of the photomixer antenna is increased. This is because the RLL adds series resistances between the probe pads and antenna. Typically, the total resistance is in the order of 5 kΩ-to-30 kΩ. Considering that DC photoconductance of the photomixers is in the order of $(10\ \text{k}\Omega)^{-1}$ [26], the bias voltage should be roughly increased by 1/2 to 3 times of its original value. It is important to keep in mind that, the effective DC voltage seen by antenna remains unchanged, and hence, the operation of the antenna is not affected by the addition of the RLL bias lines.

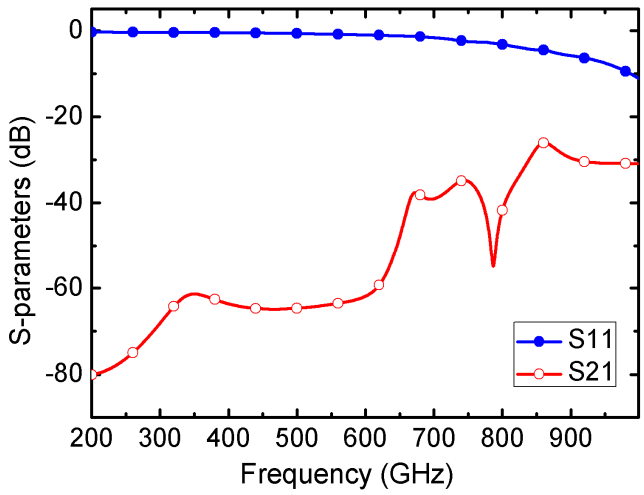

Figure 3.6 Two-port simulation results of RLL.

CHAPTER 4

ANTENNAS WITH BIAS LINES

In this chapter, several antennas with different types of bias lines are investigated numerically to observe the effects of each bias line on antenna radiation performance. Firstly, some important parameters of antenna are given, and then antennas are designed first without the presence of any bias lines. Once the antenna performances are clearly understood then each of the bias lines is connected to the designed antenna in order to investigate their effects on the performance of the antenna.

4.1. Basic Antenna Theory

In order to select and design antenna integrated with bias lines, design theories have to be well understood. For this purpose, this subsection is devoted to introduce some basic antenna parameters. Here, the most important parameters are considered and explained, and an overview of each is essential to describe antenna's performance.

4.1.1 Radiation Pattern

The radiation pattern is a graphical (three-dimensional or two-dimensional) or a mathematical illustration of the radiation properties of an antenna as a function of the space coordinates defined by the spherical coordinates (θ, φ, r) as shown in Figure 4.1, where θ is elevation plane and φ is the azimuth plane. It is mostly determined in the far field region where the spatial (angular) distribution of the radiated power does not depend on the distance. Radiation pattern gives the power that is radiated or received by a transmitting or a receiving antenna, respectively, using the angular distribution already referred. Usually, the pattern describes the normalized field (power) values with respect to the maximum values. An antenna can have one of the three types of radiation patterns

such as; isotropic, directional and omni-directional [58]. An antenna can be called as 'Isotropic' if it has the same radiation pattern in all direction. This type of pattern is called as a hypothetical lossless antenna model which can be considered as an ideal model but not physically realizable. The term 'isotropic' is usually taken as the reference while expressing the directive properties of any antenna. If an antenna can send/receive radiation energy more efficiently in one or multiple directions than other directions then it's called the directional antenna. The omni-directional antenna is one kind of directional antenna which has a constant (or directional) beam in one plane (θ or φ plane) and non-directional in the other plane [58]. The radiation pattern of an antenna is many times characterized by its lobes (or beams). The part that concentrates more radiation is often referred to main lobe. All the other lobes are called minor lobes, but some of them can have a more specific name also. When some lobe also radiates (although in a second plan) in another direction than the main lobe, it is called as side lobe. At last, there are so-called back lobes which make an angle of approximately 180° to the main beam.

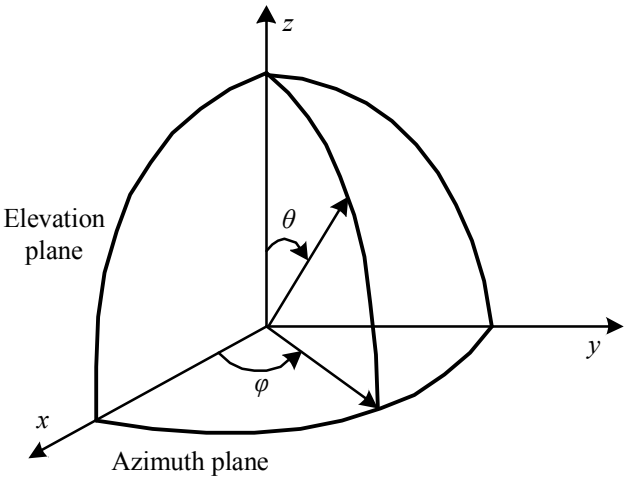

Figure 4.1 Spherical coordinate system.

4.1.2 Directivity

The term 'directivity' can be defined as the ratio of the radiation intensity in a given direction from the antenna to the radiation intensity averaged over all directions and if in that given direction the radiation intensity is maximum than it is called the maximum directivity. The analytical expression can be defined as [58]:

$$D = \frac{U}{U_0} = \frac{4\pi U}{P_{rad}} \tag{4.1}$$

where

D - directivity;

U - concentration of radiated power in a specific direction;

U_0 - concentration of radiated power of an isotropic reference;

P_{rad} - total radiated power.

Note that U_0 is given by:

$$U_0 = \frac{P_{rad}}{4\pi} \tag{4.2}$$

If there is no directivity in a specific direction, it means that the radiated power will be distributed uniformly in all directions; therefore it is referred as isotropic reference.

Otherwise, there will be directivity in a specific direction if the concentration of power radiated in that direction is bigger than the one of an isotropic reference.

4.1.3 Gain

The gain is expressed as the ratio of the power radiated by an antenna in a particular direction to the power that would be radiated if the supposed antenna was radiating isotropically, emitting the total forward accepted power (at the input terminals) instead of the total radiated power (at the output terminals), as in directivity. Also, that forward power is divided by a term 4π. Therefore, while in directivity a lossless antenna is implicit; in gain the losses are considered. This is commonly referred as to absolute gain, and it is given by the following formula:

$$G_{abs} = \frac{U}{U_0} = \frac{4\pi U}{P_{in}} \tag{4.3}$$

where

G_{abs} - gain of the antenna;

U - power radiated in a given direction;

U_0 - power that would radiate isotropically;

P_{in} - forward accepted (input) power.

Now, the relationship between gain and directivity is specified by:

$$G = \varepsilon_r \cdot D \tag{4.4}$$

where:

G - relative gain or absolute gain;

ε_r - antenna radiation efficiency;

D - directivity.

The radiation efficiency comes as:

$$\varepsilon_r = \frac{P_{rad}}{P_{in}} \tag{4.5}$$

where:

P_{rad} - total radiated power

Thus, radiation efficiency parameter gives an idea of how much power is radiated by an antenna when compared to the power that was delivered to the input terminals. The bigger is the radiation efficiency, the bigger is the gain for the same directivity.

4.1.4 Input Impedance

The input impedance of an antenna is the measure the ratio of the voltage to the current at its input terminals. Basically, those terminals are a transition between the transformation of the electric current produced by the transmitter and the

electromagnetic (EM) waves that will be radiated, work as a load to the transmission line; therefore, the input impedance is a characteristic that describes and gives an idea of how powerful the radiation will be, once it is possible to calculate the maximum power that is transmitted to the antenna before emitting the EM waves. The general expression of input impedance is given by:

$$Z_{in} = R_A + jX_A \tag{4.6}$$

where:

Z_{in} - input impedance in ohms (Ω);

R_A - antenna resistance in ohms (Ω);

X_A - antenna reactance in ohms (Ω).

All these values are pointed to the input terminals of the antenna. R_A is:

$$R_A = R_L + R_r \tag{4.7}$$

where:

R_L - loss resistance in ohms (Ω);

R_r - radiation resistance in ohms (Ω).

As shown above, input impedance is the sum of a real number and of an imaginary number. The first specifies the power that antenna radiates or the power that antenna takes in, while the imaginary part specifies the power that is not radiated by the antenna, thus retained not far away from its terminals.

4.2. Dipole Antenna

A Dipole antenna is the simplest and most widely used class of antennas. Basically, it consists of two conductive elements such as metal wires within a fed between them. They are usually named by their wire longs in wavelength [58]. In planar antennas, the calculation of a dipole length is also dependent to property of substrate, in which the relation can be given in terms of ε_{eff} by;

$$\varepsilon_{eff} = \frac{\varepsilon_r + 1}{2} + \frac{\varepsilon_r - 1}{2} \cdot \left[\left(1 + \frac{12h}{w} \right)^{-0.5} + 0.04 \cdot \left(1 - \frac{w}{h} \right)^2 \right] \quad \textbf{(4.8)}$$

where ε_r is the relative dielectric constant of substrate, h is the thickness of the substrate and w is the width of the dipole trace. Throughout this thesis study, Gallium Arsenide (GaAs), which has a ε_r = 12.8, is chosen as a host material for antennas and bias lines. Thus, effective permittivity is calculated from (4.8) as ε_{eff} = 7.2. Moreover, the wavelength in planar antennas can be calculated as $\lambda_0 / \sqrt{\varepsilon_{eff}}$,where λ_0 is the free space wavelength.

As a first test structure for bias lines, a λ-long dipole antenna operating at a center frequency of 400 GHz is designed (Figure 4.2). In order to achieve the specified operation frequency, the length of dipole is tuned. The design parameters of the dipole antenna and bias lines are given in Table 4.1. In order to calculate the average impedance of designed dipole antenna with no bias line, Schnelkunoff's approach is

utilized, which is firstly reported by [60]. In this approach, the two arms of printed dipole antenna are modeled as two conductors of transmission line and the characteristic impedance of antenna is adopted as;

$$Z_0 = \frac{120}{r_2 - r_1}\left[r_2\left(\ln\left(\frac{8r_2}{w}\right) - 1\right) - r_1\left(\ln\left(\frac{8r_1}{w}\right) - 1\right)\right] \quad \textbf{(4.9)}$$

By using the design parameters of dipole antenna listed in Table 1, the impedance of dipole is calculated by using (4.9) and a value of 570 Ω is obtained.

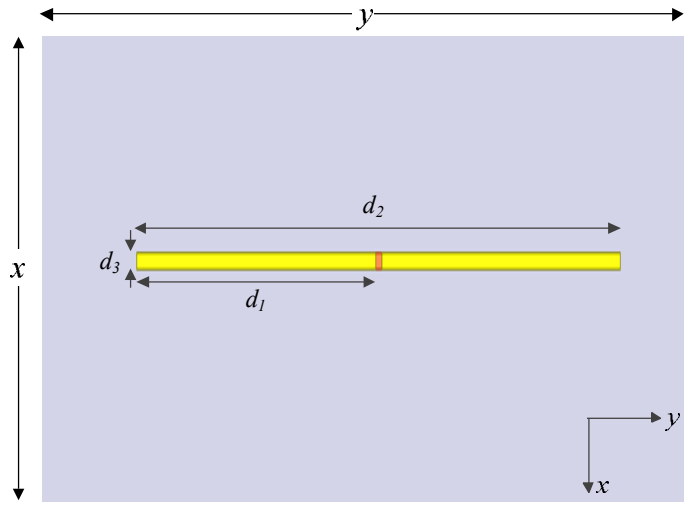

Figure 4.2 The layout of the designed dipole antenna.

Table 4.1 The design parameters of the dipole antenna.

Antenna and substrate parameters				*Bias line parameters*			
Parameter	Value (μm)	Parameter	Value (μm)	Parameter	Value (μm)	Parameter	Value (μm)
d_1	114.5	x	600	a	1	d	60
d_2	232	y	400	b	70	e	70
d_3	3			c	2	r	1

Once the characterization of dipole antenna in terms of design parameters and impedance calculation are achieved, the simulations of antenna with different bias lines are conducted, and the results are illustrated in Figure 4.3. Note that, the simulation procedure described in Chapter 2 is followed during the numerical work in this chapter. Once can see from simulation results that the impedance of antenna with no bias line is 428 Ω at 399 GHz. In addition, it can be clearly seen that the CPS and PBG bias lines change the antenna impedance and operation frequency, whereas RLL bias line keeps the operation frequency almost the same with the original antenna. It is also observed that the RLL bias line hardly affects the radiation pattern while the former two types distort the radiation pattern. This behavior can be more clearly understood once the current distributions are examined for all cases. The current distributions at highest intensity of each bias line are presented in Figure 4.4. When CPS bias line is used, a considerable amount of current leakage is noted on the bias lines; moreover, a standing wave pattern is clearly observed as expected, proving the transmission line behavior (Figure 4.4-(a)). Although the amount of current leakage on the bias line decreases when the PBG bias line is used (Figure 4.4-(b)), it still has a notable effect on antenna radiation pattern (Figure 4.3-(b)). On the other hand, the intensity of current leakage on the bias lines are reduced extensively when the RLL bias line is selected, and therefore, having the closest input impedance and radiation pattern performance compared to that of the no bias line scenario is explained.

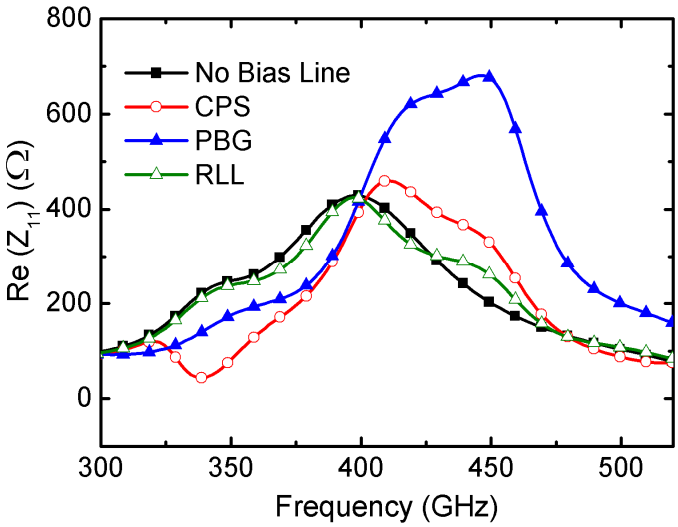

a) Real part of the input impedance

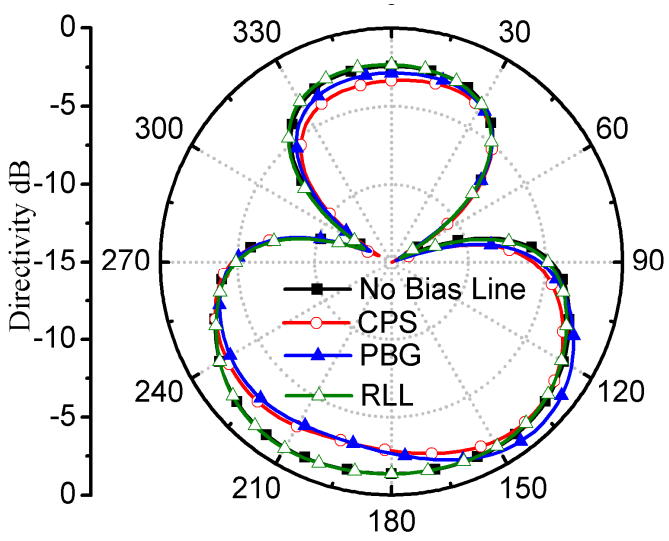

b) directivity (at 398.5 GHz)

Figure 4.3 (a) to **(b)** The simulation results of dipole antenna.

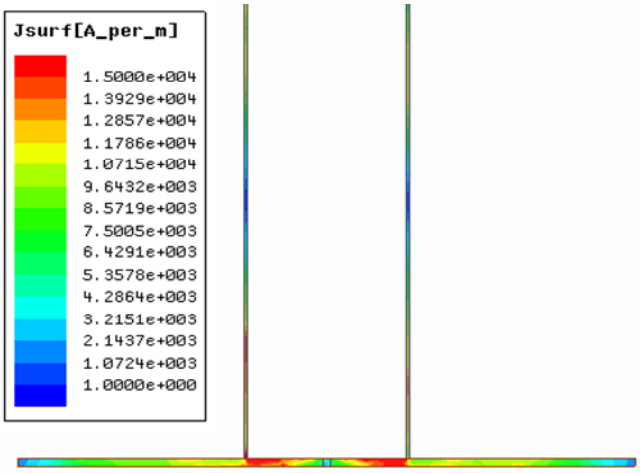

a) Dipole antenna with CPS

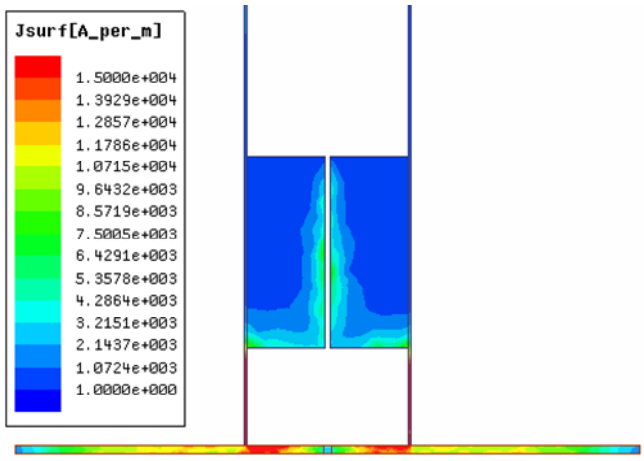

b) Dipole antenna with PBG

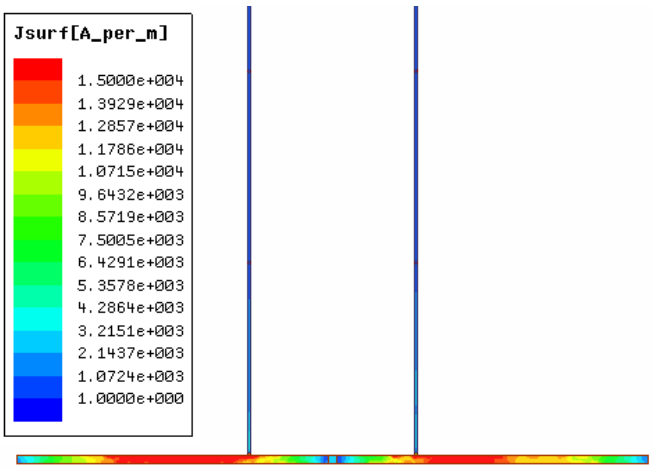

c) Dipole antenna with RLL

Figure 4.4 (a) to **(c)** The current distributions of dipole antenna with bias lines at 398.5 GHz.

4.3. Folded Dipole Antenna

Folded dipole antennas (see Figure 4.5) are also employed as photomixer antennas due to their nature of having high radiation resistance. In a standard dipole the currents flowing along the conductors are in phase and as a result there is no cancellation of the fields and radiation occurs. When the second conductor is added to make the folded dipole antenna this can be considered as an extension to the standard dipole with the ends folded back to meet each other. As a result the currents in the new section flow in the same direction as those in the original dipole. The currents along both the half-waves are therefore in phase and the antenna will radiate with the same radiation patterns as a simple half-wave dipole. The impedance increase can be deduced from the fact that the power supplied to a folded dipole antenna is evenly shared between the two sections which constitute the antenna. This means that when compared to a standard dipole the current in each conductor is reduced to a half. As the same power is applied, the impedance has to be raised by a factor of four to retain balance in the equation $Watts = I^2 \times R$. In addition, the spacing between two sections of folded dipole is essential for operating frequency. In order to clarify this effect, folded dipole antennas with different length of spacing are designed and simulated. The variation of spacing length is altered between 3 μm and 20 μm. One can say from the simulation results illustrated in Figure 4.6 that the operating frequency is shifted to low frequencies while increasing the spacing between arms (S1 to S5 from figure 4.6). Hence, the design that has an operating frequency at 400 GHz (length of spacing = 15 μm) is selected in order to understand the behavior of folded dipole antenna with bias lines. The exact design parameters of antenna and bias lines can be found in Table 4.2. The same calculation and simulation steps for the dipole antenna are also applied for the folded dipole antenna, and simulation results are illustrated in Figure 4.7. It is seen that the CPS and PBG bias lines reduce the radiation resistance considerably, shift the operating frequency, and narrow the bandwidth of the antenna (Figure 4.7-(a)). On the other hand, the RLL bias line causes a much lower radiation resistance drop and operating frequency shift, and the bandwidth of the antenna stays almost the same.

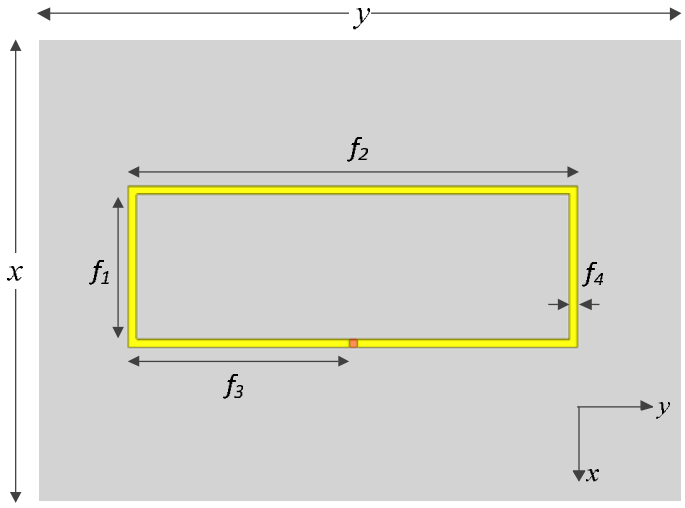

Figure 4.5 The layout of the designed folded dipole antenna.

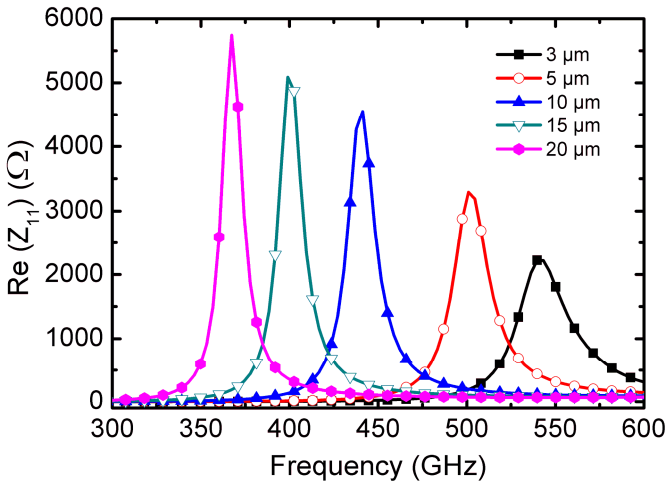

Figure 4.6 Folded dipole antenna with different spacing lengths

Additionally, the CPS and PBG bias lines distract the radiation pattern of the antenna (Figure 4.7-(b)) due to the considerable amount of the current leakage on the bias lines (Figure 4.8-(a) and Figure 4.8-(b)), while the RLL bias line shows quite similar behavior with the radiation pattern of original antenna, since the current leakage is blocked by lumped resistances (Figure 4.8-(c)). As a result, one can say that the RLL bias line gives a satisfactory improvement compared to the previous two types of bias lines for the folded dipole antenna.

Table 4.2 The design parameters of the folded dipole antenna.

Antenna and substrate parameters				*Bias line parameters*			
Parameter	Value (μm)	Parameter	Value (μm)	Parameter	Value (μm)	Parameter	Value (μm)
f_1	15	x	600	a	1	d	20
f_2	58	y	400	b	70	e	70
f_3	28.5			c	1	r	1

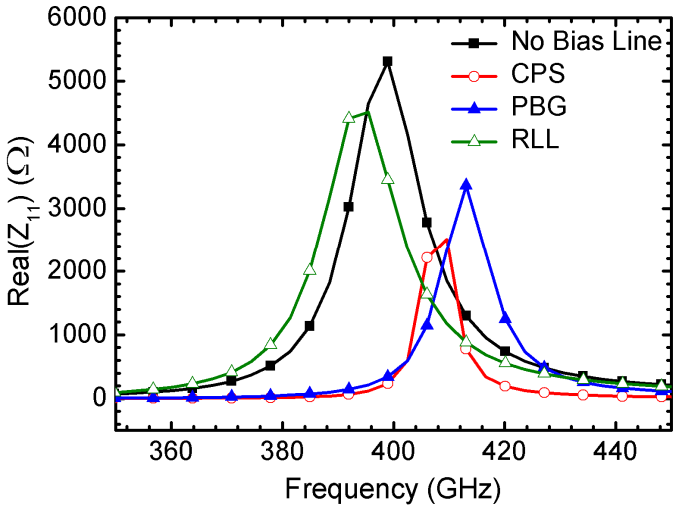

a) Real part of input impedance

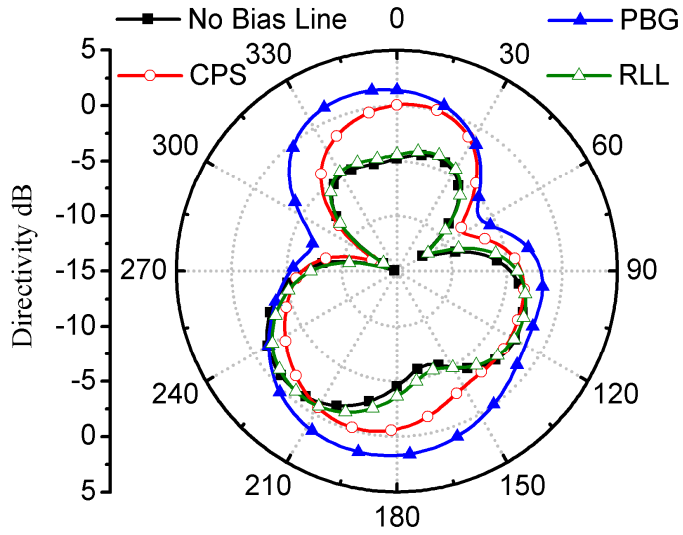

b) directivity (at 399 GHz)

Figure 4.7 (**a)** to (**b)** The simulation results of folded dipole antenna.

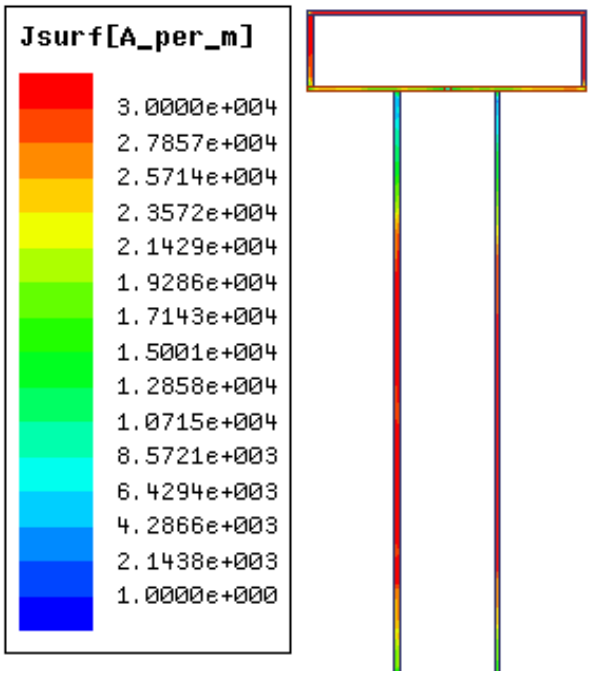

a) Folded dipole antenna with CPS

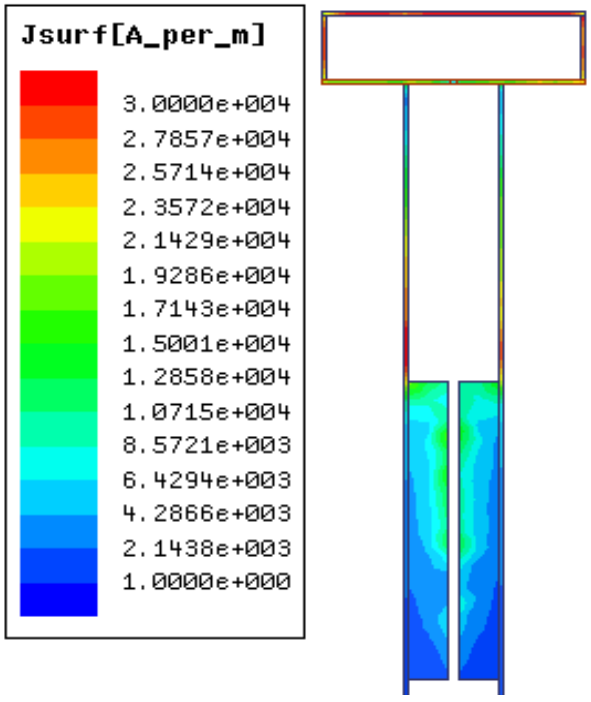

b) Folded dipole antenna with PBG

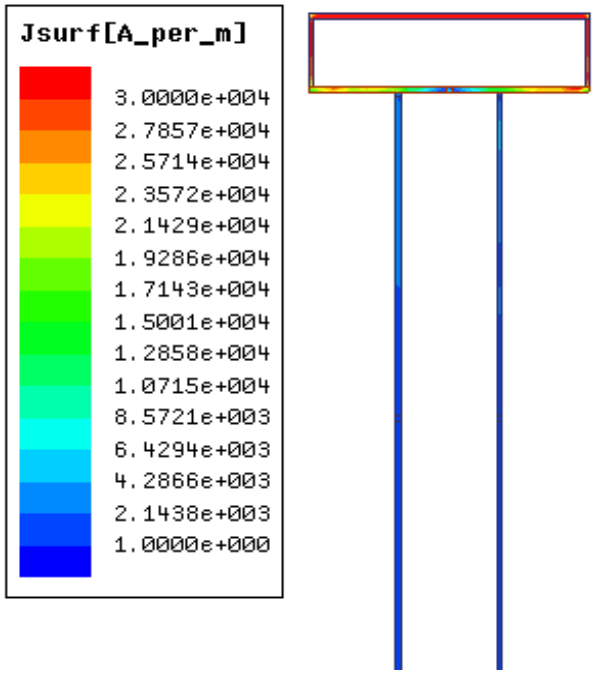

c) Folded dipole antenna with RLL

Figure 4.8 (a) to **(c)** The current distributions of folded dipole antenna with bias lines at 399 GHz.

4.4. Archimedean Spiral Antenna

The effects of bias lines on frequency independent antennas are also investigated. An antenna that can be completely specified by angles is frequency independent [61], which means that antenna impedance and radiation properties depend on the shape and dimensions expressed in wavelengths. The archimedean spiral antenna is one of the popular of frequency independent antenna, hence a self- complementary archimedean spiral antenna with tapered end is chosen as test structure for bias lines. A spiral antenna, which is depicted in Figure 4.9 and dimensions are given in Table 4.3, is self-complementary if the patch and air regions of the antenna are equal. Each arm of an archimedean spiral is linearly proportional to the angle, ϕ, and is described by the following relationships

$$r = r_0\phi + r_1 \qquad \textbf{(4.10)}$$

where r_1 is the inner radius of the spiral. The proportionality constant is determined from the width of each arm, *w*, and the spacing between each turn, *s*, which for a self complementary spiral is given by

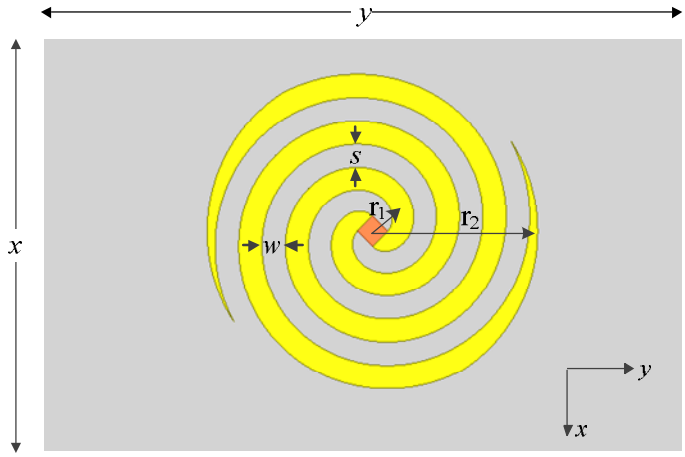

Figure 4.9 The layout of the designed spiral antenna.

Table 4.3 The design parameters of the spiral antenna.

Antenna and substrate parameters				*Bias line parameters*			
Parameter	Value	Parameter	Value (degree)	Parameter	Value (μm)	Parameter	Value (μm)
r_1	2 μm	x	500	a	2	d	165
Offset angle	90°	y	500	b	62	e	60
				c	1	r	2

$$r_0 = \frac{s+w}{\pi} = \frac{2w}{\pi} \tag{4.11}$$

The strip width of each arm can be found from the following equation

$$s = \frac{r_2 - r_1}{2N} - w = w \tag{4.12}$$

If the structure is self-complementary structure then (4.12) can be written as

$$s = w = \frac{r_2 - r_1}{4N} \tag{4.13}$$

where r_2 is the outer radius of the spiral and N is the number of turns.

The Archimedean spiral antenna radiates from a region where the circumference of the spiral equals one wavelength. This is called the active region of the spiral. Each arm of the spiral is fed 180° out of phase, so when the circumference of the spiral is one wavelength the currents at complementary or opposite points on each arm of the spiral add in phase in the far field. The low frequency operating point of the spiral is determined theoretically by the outer radius and is given by

$$f_{low} = \frac{c}{2\pi r_2} \tag{4.14}$$

where c is the speed of light. Similarly the high frequency operating point is based on the inner radius giving

$$f_{high} = \frac{c}{2\pi r_1} \tag{4.15}$$

In practice the low frequency point will be greater than predicted by (4.14) due to reflections from the end of the spiral. The reflections can be minimized by using resistive loading at the end of each arm or by adding conductivity loss to some part of the outer turn of each arm. Also, the high frequency limit may be less than found from (4.15) due to feed region effects.

The simulation conditions for previous antennas are also applied to the spiral antenna. The simulation results in Figure 4.10-(a) show that the antenna has an input impedance of 2337 Ω at 468 GHz when no bias lines are connected. It is clearly observed from the simulation results that the input impedance is severely reduced in case of using the CPS and PBG bias lines. The input impedance for the CPS and PBG bias line cases are 279 Ω and 174 Ω (both measured at 492 GHz), respectively. Alternatively, the RLL bias line results in an input impedance of 1776 Ω, which is 6 times and 10 times better than that of the CPS and PBG bias lines, respectively; moreover, it keeps the operating frequency at almost same value compared to the original antenna with no bias lines. The current distributions for all three types of bias lines are shown in Figure 4.11 in order to see their effects clearly on the antenna performance. It is seen from the simulations results that the CPS and PBG bias lines have a significant intensity of current leakage into the bias lines (Figure 4.11-(a) and Figure 4.11-(b)), and as a result, the radiation patterns of the antennas with these bias lines have considerable changes (Figure 4.10-(b)). On the other hand, the current leakage into bias line is minimized when the RLL bias line is used, and the radiation pattern remains almost the same compared to the original antenna with no bias lines. As a result, one can say that the proposed RLL bias line gives the closest performance among three types of bias lines compared to the original antenna with no bias lines.

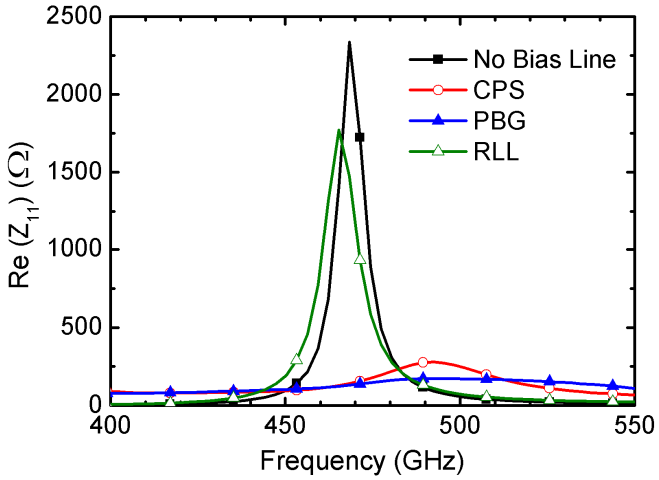

a) Real part of the input impedance

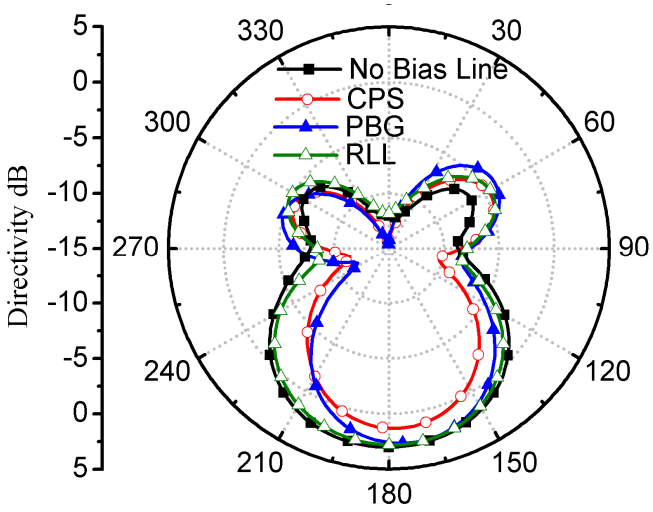

b) directivity (at 468 GHz)

Figure 4.10 (**a)** to (**b)** The simulation results of spiral antenna.

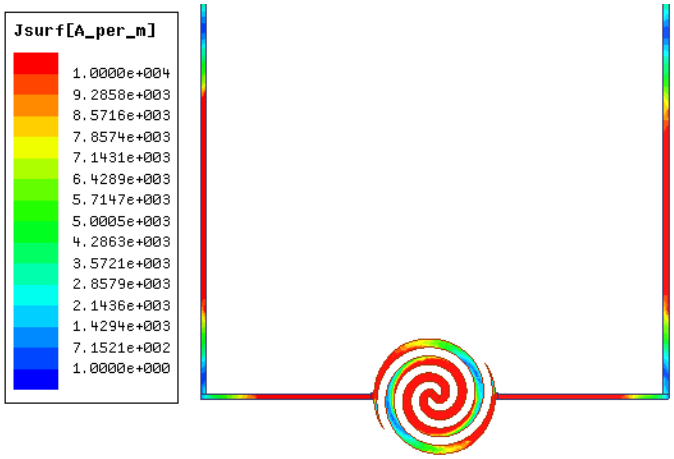

a) Spiral antenna with CPS

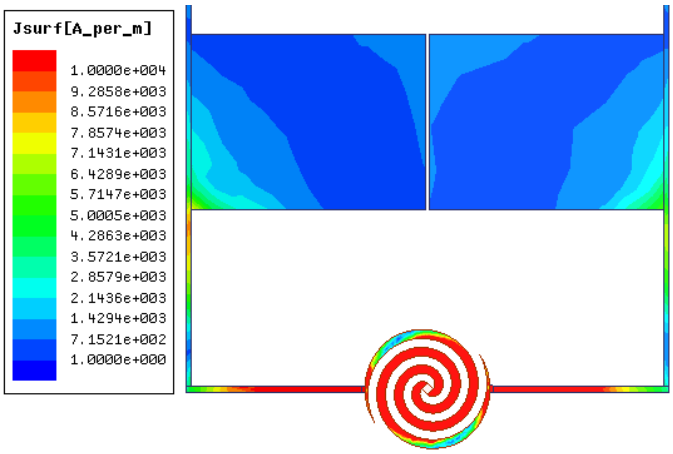

b) Spiral antenna with PBG

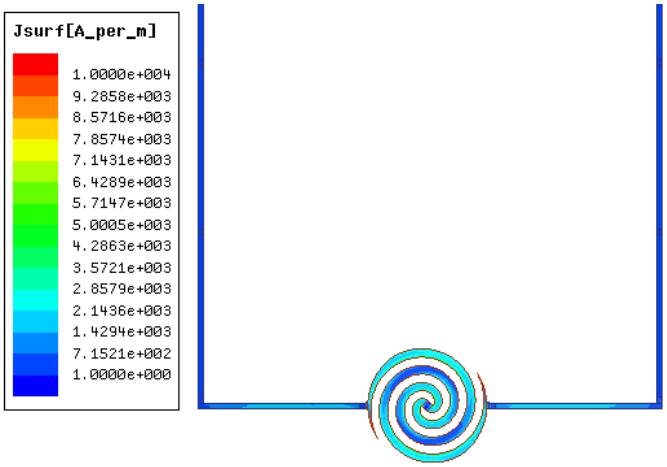

c) Spiral antenna with RLL

Figure 4.11 (a) to **(c)** The current distributions of spiral antenna with bias lines at 468 GHz.

One can also keep in mind that the investigated spiral antenna exhibits as an one turn spiral antenna's property [62]. Naturally, frequency independent antennas exhibit impedance over a wide band frequency spectrum. However, in order to obtain a high impedance of spiral antenna, the turn numbers of antenna is reduced. To prove this idea, spiral antennas that possess different turn numbers are designed and simulated. One can see from simulation results shown in Figure 4.12 that if the turn numbers are greater than 2 turns for designed spiral antenna, it behaves as a frequency independent antenna as explained at the beginning of this subsection. However, if the turn number of spiral antenna is reduced to 2 or less, the spiral antenna will exhibit high impedance at a certain frequency. Since high impedance antennas are needed in photomixer design (as explained in Chapter 1), 1.6 turns spiral antenna is chosen for testing the bias line in this thesis.

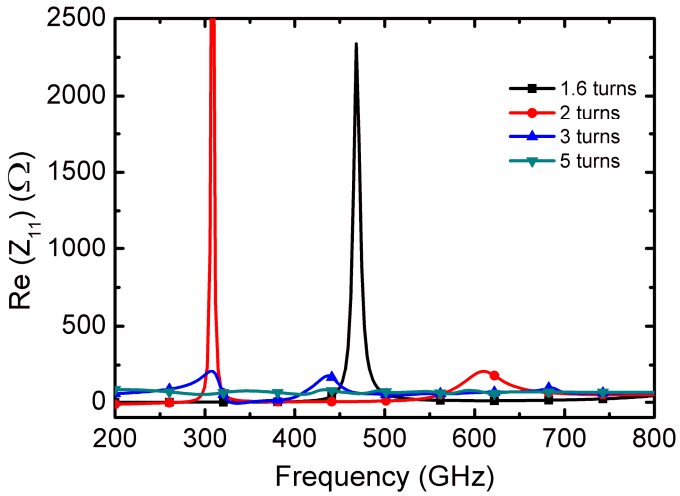

Figure 4.12 Archimedean spiral antennas with different turn numbers.

4.5. Log-periodic Antenna

The log-periodic antenna is also one of the popular of frequency independent antenna, hence a self- complementary log-periodic antenna is chosen as test structure for bias lines. A log-periodic antenna is self-complementary if the patch and air regions of the

antenna are equal and the angles of antenna should fulfill the condition $\delta + \beta = 90^0$. There are three basic design principles that symbolize the logarithmically periodic antenna whose properties vary periodically with the logarithm of the frequency. The first one is the angle concept. In this design concept, the geometry of the antenna structure is completely described by angles rather than lengths, δ and β angles as shown in Figure 4.13. The second principle is that input impedance and radiation pattern of this type of antenna vary periodically with the logarithm of the frequency [64]. The third principle is to design the antenna structure where its electrical properties repeat periodically with the logarithm of the frequency.

The layout of a trapezoidal-toothed log-periodic antenna, which is investigated in this study, is given in Figure 4.13. It can be seen that the arms of log-periodic antenna are rotated version of each other. The number of teeth on each side of the center strip (angular dimension β) should be the same as stagger spaced. Defining R_n as the distance from the vertex to the edge of the n^{th} tooth of one side of strip (n =1 for outer tooth) and t_n as the distance from the vertex to the edge of the n^{th} tooth of the other side of the strip, the scaling ratio for the structure is defined as;

$$\tau = \frac{R_{n+1}}{R_n} \tag{4.16}$$

and the spacing factor is characterized by

$$\sigma = \frac{t_n}{R_n} \tag{4.17}$$

With respect to the logarithm of frequency, the input impedance has a period $\sqrt{\tau} = 0.836$. It should be noted that the number of teeth specify the number of resonance occurred. Hence the designed log periodic antenna is simulated and the result illustrated in Fig 4.13 indicates that designed antenna is operating between 0.4-1.2 THz

and six teeth of log periodic antenna excite six resonance behaviors. These resonances follow the approximate periodicity of $\sqrt{\tau} = 0.836$, which is a natural result of log-periodic geometry of antenna. Here, the designed antenna is investigated between a frequency spectrum of 300-750 GHz.

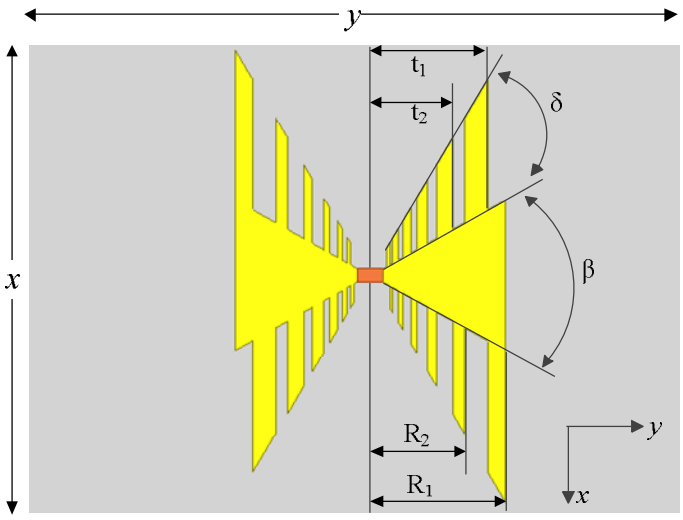

Figure 4.13 The layout of the designed log periodic antenna.

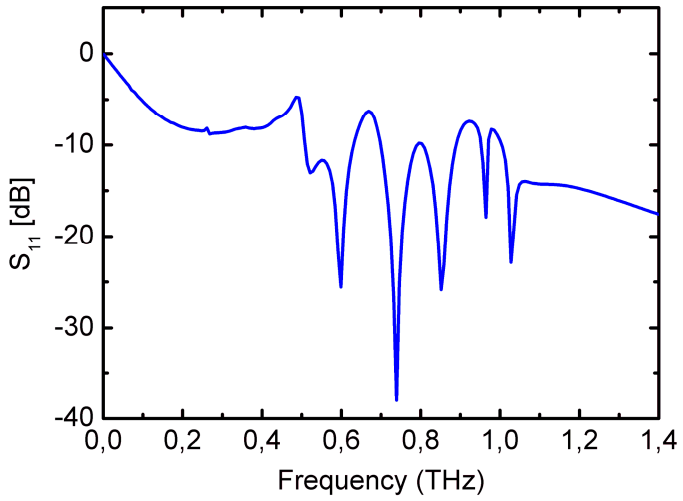

Figure 4.14 Computed return loss of log periodic antenna

As it is explained at the beginning of this section, self-complementary antennas exhibits frequency independent impedance which is based Babinet's principle and can be given as;

$$Z_A = \frac{Z_0}{2\sqrt{\varepsilon_{eff}}} \tag{4.18}$$

where $Z_0 = 120\pi = 370\,\Omega$ is the wave impedance in free space. The effective permittivity ε_{eff} can be deducted from (4.1) as $(\varepsilon_r + 1)/2$. For GaAs substrate $(\varepsilon_r = 12.8)$ the impedance Z_A can be calculated from (4.18) as 72 Ω.

In order to investigate the RLL bias line performance in log periodic antenna, the bias lines are connected to the antenna and simulation for each of them is accomplished. The design parameters are given in Table 4.4. The simulation setup defined previously is also followed for log periodic antenna. Firstly, it can be seen from Figure 4.15-(a) that when CPS and PBG bias lines are connected to the log-periodic antenna, they distort the antenna characteristics. In addition, the resonance frequencies are shifted and the radiation resistances are reduced significantly, especially for the third resonance around 670 GHz. The radiation patterns are also affected, which can be seen in Figure 4.15-(b) as an example. The current distributions at highest intensities shown in Figure 4.16 also support and verify the observation where a strong leakage current is observed for the CPS and PBG bias line cases and almost no leakage current is observed for the RLL bias line case. Comparing all three results, one can conclude that using RLL bias lines improves the log-periodic antenna performance compared to the CPS and PBG bias line cases and gives the closest results to that of the original antenna with no bias lines.

Table 4.4 The design parameters of the log periodic antenna.

Antenna and substrate parameters				*Bias line parameters*			
Parameter	Value (μm)	Parameter	Value	Parameter	Value (μm)	Parameter	Value (μm)
x	600	δ	30^0	a	2	d	62
y	400	β	60^0	b	42.5	e	42.5
length	52	τ	0.7	c	1.5	r	2
		σ	0.87				

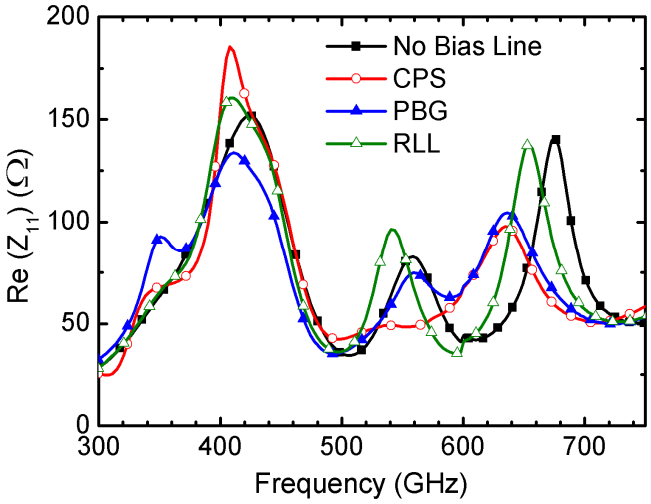

a) Real part of the input impedance

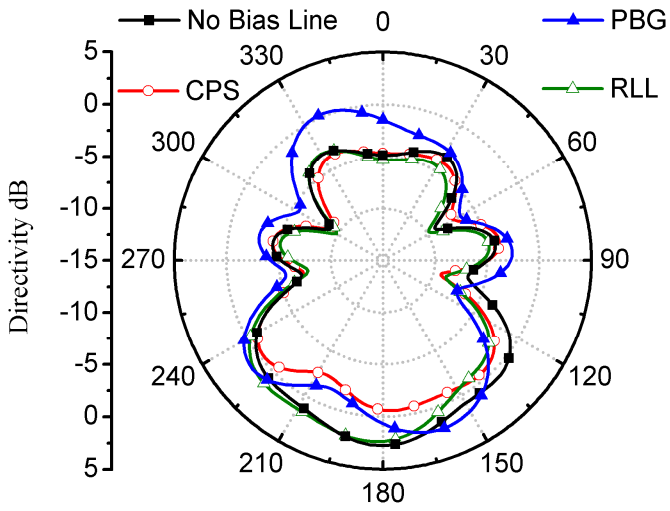

b) directivity (at 558 GHz)

Figure 4.15 (**a**) to (**b**) The simulation results of log periodic antenna.

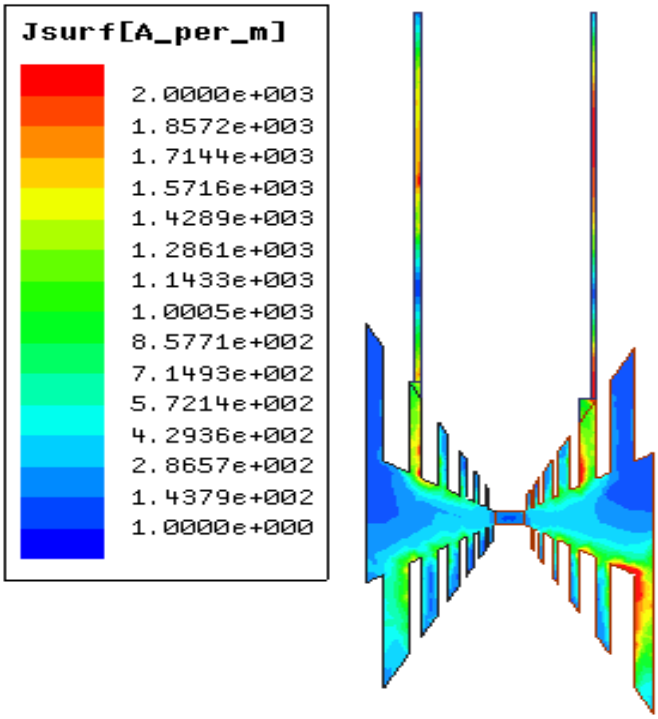

a) Log periodic antenna with CPS

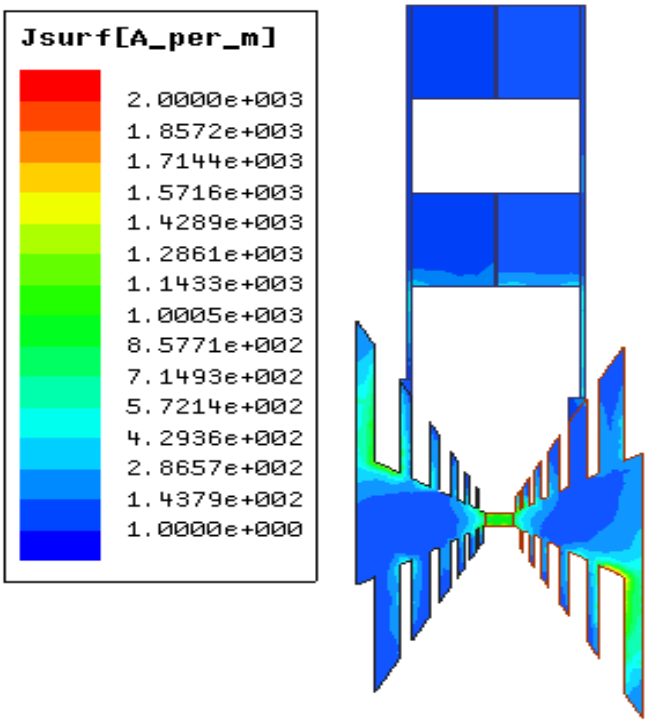

b) Log periodic antenna with PBG

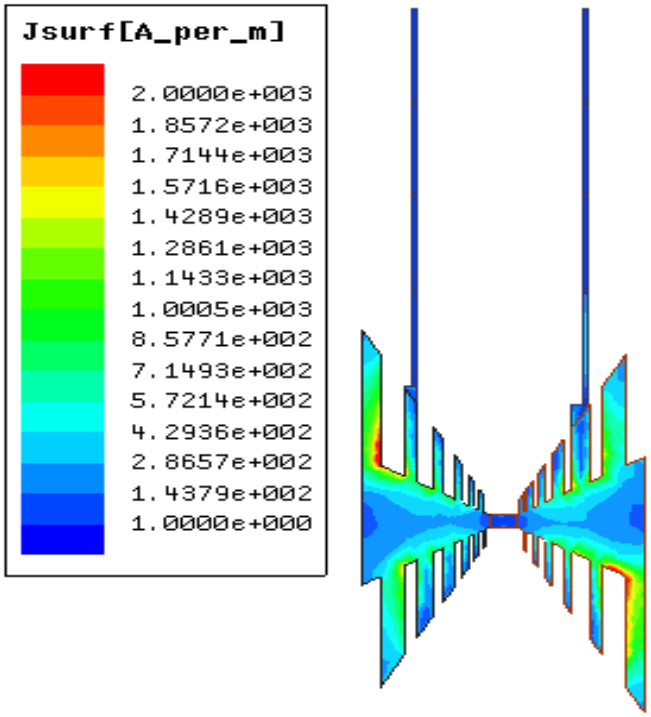

c) Log periodic antenna with RLL

Figure 4.16 (a) to **(c)** The current distributions of log periodic antenna with bias lines at 426 GHz.

4.6. The Effects on Radiation Efficiency

It is expected that the lumped resistances used in the RLLs affect the radiation efficiency of the antenna. As mentioned previously, antenna metals are modeled as PECs in order to see the effects of the RLLs clearly on the antenna efficiency. It is observed from the simulation results of the four antennas that the radiation efficiency is reduced at most 2% when RLL bias lines are employed, and the radiation efficiency can be increased further by increasing the value of the lumped resistances. In order to clarify this idea, the designed folded dipole antenna in Section 4.3 is chosen as a test structure for different values of lumped resistance, which is varied between 250 Ω –to- 30 kΩ. The simulation results are shown in Figure 4.17, where one can see that when the lumped resistance value is increased the performance of antenna with RLL is getting closer to antenna performance with no bias line. Also, one should note that the

increasing the value of resistance does not affect the voltage seen by the antenna, which means that the operation of the antenna remains unaffected.

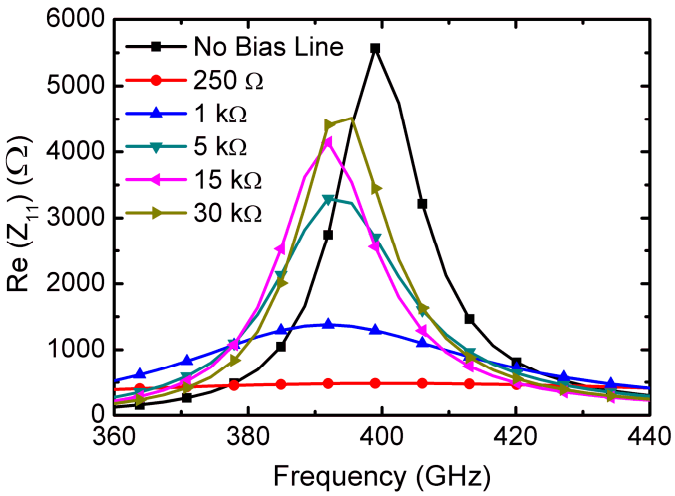

Figure 4.17 Folded dipole antenna with different values of lumped resistance

It should also be underlined once more here that the usage of the lumped resistances effectively blocks the leakage current formed on the bias lines. This is an important result because the leakage currents on the thin, narrow, and long bias lines is expected to cause a considerable amount of resistive power loss, which will decrease the antenna efficiency notably. It is observed from the simulations that increasing the value of resistance significantly effects the antenna efficiency, which is a direct consequences of reducing the current leakage into bias lines, hence the closest performance to antenna with no bias line is achieved when using the highest value of lumped resistance. During this study, the lumped resistances for each antenna are selected starting from 1 kΩ as resistance values less than 1 kΩ did not provide good isolation. Although resistance values up to 30 kΩ are applied for different types of antennas, a resistance level of a few kΩ is sufficient to provide good isolation and recover the original antenna performance (without any bias lines) for most of the cases.

CHAPTER 5

CONCLUSION

In this research, a novel DC bias line, namely resistively loaded line (RLL), is introduced to photomixer antennas. Among the performance affecting factors in photomixer antennas, DC bias lines are taken into consideration during this thesis. Therefore, the bias lines that exist in literature are reviewed firstly. Coplanar stripline (CPS) and photonic bandgap (PBG) type bias lines are mostly being used in photomixer systems. RLL type bias line is proposed for photomixer antennas. Basic theoretical background of these bias lines is studied and their two-port network is outlined in order to understand their behavior when they are implemented in a photomixer design. Advantages and disadvantages of each bias line are discussed. Once the characterizations of bias lines are obtained, their applications to antennas are numerically studied. In order to compare each performance of bias line, various antennas are designed and numerical study on them is carried out.

HFSS is chosen as designing tool and numerical simulation method for this thesis. Since accurate simulation depends on proper choice of solution parameter in HFSS, some of main parameters with various boundary conditions are investigated in this thesis. It is observed that reducing the max delta S, one of the main solution parameter to be specified in HFSS, will increase the mesh number, hence the simulation time will be naturally increase, but more accurate results will be obtained. In addition, it is seen that PML and ABC boundary conditions will give exactly same results when their airbox distance to substrate is properly specified. The outcomes of these studies are taken into consideration during all simulation studies throughout this thesis.

Types of bias lines are studied in terms of two-port network equivalent of each of them. CPS is one of the well known structure and its characterization is well studied. A CPS

design, which has a characteristic impedance of 197.8 Ω, is investigated. It is seen that it exhibits a typical transmission line behavior, hence it will be the worst candidate for achieving isolation of probe pads and antennas when they are used in a photomixer system. PBG type bias line takes place in order to reduce the current leakage into the bias lines. A PBG design is investigated in this study and it is observed that it operates as a low pass filter by virtue of holding high/low impedance sections through the bias line. Although the designed PBG provides isolation above 200 GHz, when it is used in with photomixer antennas it fails to preserve the performance of antenna with no bias line due to the large metal sections inserted into photomixer system. RLL type bias line is proposed due to the challenges discussed above. A RLL design is investigated with varying the impedance values. It is observed that it provides isolation between probe pads and antenna even the values of impedance is reduced to 20 Ω.

The effect of each bias line on photomixer antenna is investigated. For this purpose, various antennas such as dipole, folded dipole, spiral, and log-periodic antennas are designed as test structures of bias lines. Dipole antenna is one of the most popular photomixer antennas. For that reason, a dipole antenna that operates at 400 GHz is chosen as a first test structure for bias lines. The designed dipole antenna itself exhibits an impedance value of 428 Ω. The simulation results of dipole antenna indicate that the closest performance to antenna with no bias line case is achieved by RLL. Next, folded dipole antenna takes places in photomixer systems due to its nature of having high radiation resistance. It is showed that the impedance value increases and operating frequency is decreases when the length between the two arms of folded dipole antenna is increased. A folded dipole design that operates at 400 GHz is chosen as a test structure for bias lines, and it is observed that the antenna radiation characteristics barely effected when RLL type bias lines are used. In order to see effects of bias lines on frequency independent antenna, two of them, namely archimedean spiral and log periodic antennas, are designed. The investigated spiral antenna exhibits one turn

impedance property and gives an impedance of 2337 Ω at 468 GHz. Since the high impedance of antennas is essential in photomixer system the designed spiral antenna is chosen for bias lines. It is observed that the antenna with CPS and PBG designs exist impedances as 279 Ω and 174 Ω, respectively. On the other hand, RLL gives an impedance values of 1776 Ω, which is 6 times and 10 times better than that of the CPS and PBG bias lines, respectively. The investigated log periodic antenna is a 6 toothed antenna, which indicates the reason of 6 resonances between 0.4 – 1.2 THz. When the CPS and PBG type bias lines are connected to the log-periodic antenna, it is seen that they distort the antenna characteristics, and the resonance frequencies are shifted. The effects of bias lines on all of aforementioned antennas can be more clearly understood when the current distributions are investigated. Since the CPS and PBG type bias lines are directly connected to antenna without any precautions, there is a considerable amount of current leakage into these bias lines, which is the main reason of distortions on antenna radiation characteristics. On the other hand, RLL barely allows THz current leakage even with the low lumped impedance values. It should be carefully noted that, the RLL bias lines are formed with at least 1 kΩ lumped resistance in order to obtain the least antenna efficiency drop. However, the antenna efficiency can be improved by using lumped resistance values up to 20 kΩ. As a result, with a proper design of proposed bias line, the performance of photomixer antenna will be barely effected.

As a future work, it can be suggested that proposed bias line can be fabricated and tested with designed antennas. Then, the experimental results can be used to verify the simulation results for practical application. In addition, performance of proposed bias line can be tested for different antennas and for various frequencies.

REFERENCES

[1] Y. Lee, Principles of terahertz science and technology, (1st ed.), Springer, New York, 2008.

[2] Zhang, X. C., Jingzhou X., Introduction to THz Wave Photonics, (1st ed.), New York, 2010.

[3] Calvin, Y., Shuting, F., Yiwen, S., Pickwell-MacPherson, E., The potential of terahertz imaging for cancer diagnosis: A review of investigations to date, Quantitative Imaging in Medicine and Surgery, 2 (1), 33-45, 2012.

[4] Woodward, R. M., Wallace, V. P., Pyle, R. J., Cole, B. E., Arnone, D. D., Linfield, E. H., Pepper, M., THz pulse imaging of ex vivo basal cell carcinoma, Journal of Investigative Dermatology, 120 (1), 72–78, 2003.

[5] Kawase, K., Ogawa, Y., Watanabe, Y., Inoue, H., Non-destructive terahertz imaging of illicit drugs using spectral fingerprints, Optics Express, 11 (20), 2549-2554, 2003.

[6] Wang, J., Yang, J. Y., Fazal, I. M., Ahmed, N., Yan, Y., Huang, H., Ren, Y., Yue, Y., Dolinar, S., Tur, M., Willner, A. E., Terabit free-space data transmission employing orbital angular momentum multiplexing, Nature Photonics, 6, 488-496, 2012.

[7] Hu, B. B., Nuss, M. C., Imaging with terahertz waves, Optics Letters, 20 (16), 1716-1718, 1995.

[8] Mittleman, D. M., Jacobsen, R. H., Nuss, M. C., T-ray imaging, IEEE Journal of Selected Topics in Quantum Electronics, 2 (3), 679-692, 1996.

[9] Fitch, M. J., Osiander, R., Terahertz waves for Communications and Sensing, Johns Hopkins APL Technical Digest, 25 (4), 348-355, 2004.

[10] Kemp, M. C., Taday, P. F., Cole, B. E., Cluff, J. A., Fitzgerald , A. J., Tribe W. R., Security applications of terahertz technology, Terahertz for Military and Security Applications, 21 April 2003, SPIE, 5070, 44-52, 2003.

[11] Markelz, A., Whitmire, S., Hillebrecht, J., Birge, R., THz time domain spectroscopy of biomolecular conformational modes, Physics in Medicine and Biology, 47 (21), 3739-3805, 2002.

[12] Zeitler, J. A., Taday, P. F., Newnham, D. A., Pepper, M., Gordon, K. C., Rades, T., Terahertz pulsed spectroscopy and imaging in the pharmaceutical setting - a review, Journal of Pharmacology and Pharmacotherapeutics, 59 (2), 209-233, 2007.

[13] Rowe, D. G., Terahertz takes to the stage, Nature Photonics, 1, 75-77, 2007.

[14] Tonouchi, M., Cutting-edge terahertz technology, Nature Photonics,1, 97-105, 2007.

[15] Mukherjee, P., Gupta, B., Terahertz (THz) frequency sources and antennas - A brief review, International Journal of Infrared and Millimeter Waves, 29 (12), 1091-1102, 2008.

[16] Siegel, P. H., Terahertz technology IEEE Transactions on Microwave Theory and Techniques, 50 (3), 910-928, 2002.

[17] Ferguson, B. and Zhang X., Materials for terahertz science and technology, Nature Materials, 1, 26-33, 2002.

[18] Lewis, R. A., A review of terahertz sources, Journal of Physics D: Applied Physics, 47, 374001-374011, 2014.

[19] Williams, G. P., Filling the THz gap – high power sources and applications, Reports on Progress in Physics, 69 (2), 301-326, 2006.

[20] Saeedkia, D., Modeling and design of photoconductive and superconductive terahertz photomixer sources, Thesis (PhD), University of Waterloo, 2005.

[21] Preu, S., Döhler, G. H., Malzer, S., Wang, L. J., Gossard, A. C., Tunable, continuous-wave terahertz photomixer sources and applications, Journal of Applied Physics, 109, 061301-061356, 2011.

[22] Verghese, S., McIntosh, K. A., Calawa, S., Dinatale, W. F., Duerr, E. K., Molvar, K. A., Generation and detection of coherent terahertz waves using two photomixers, Applied Physics Letters, 73 (26), 3824-3826, 1998.

[23] Gregory, I. S., Evans, M. J., Page, H., Malik, S., Farrer, I., Beere, H. E., Analysis of photomixer receivers for continuous-wave terahertz radiation, Applied Physics Letters, 91, 154103-154105, 2007.

[24] Berry, C. W., Wang, N., Hashemi, M. R., Unlu, M., Jarrahi, M., Significant performance enhancement in photoconductive terahertz optoelectronics by

incorporating plasmonic contact electrodes, Nature Communications, 4, 1622-1632, 2013.

[25] Duerr, E. K., Distributed Photomixers, Thesis (PhD), Massachusetts Institute of Technology, 2002.

[26] Brown, E., Smith, F., McIntosh, K., Coherent millimeter-wave generation by heterodyne conversion in low-temperature-grown GaAs photoconductors, Journal of Applied Physics, 73 (3), 1480–1484, 1993.

[27] Matsuura, S., Tani, M., Sakai, K., Generation of coherent terahertz radiation by photomixing in dipole photoconductive antennas, Applied Physics Letters, 70 (5), 559–561, 1997.

[28] Matsuura, S., Ito, H., Generation of CW terahertz radiation with photomixing, Terahertz Optoelectronics, 97, 157-204, 2005.

[29] Gregory, I. S. Baker, C., Tribe, W. R., Bradley, I. V., Evans, M. J., Linfield, E. H., Davies, A. G., Missous, M., Optimization of Photomixers and Antennas for Continuous-Wave THz Emission, IEEE Journal of Quantum Electronics, 41(5), 717–728, 2005.

[30] Khiabani, N., Modelling, design and characterisation of terahertz photoconductive antennas, Thesis (PhD), University of Liverpool, 2013.

[31] Miyamaru, F., Saito, Y., Yamamoto, K., Furuya, T., Nishizawa, S., Tani, M., Dependence of emission of terahertz radiation on geometrical parameters of dipole photoconductive antennas, Applied Physics Letters, 96 (21), 211104-211106, 2010.

[32] Dragoman, D., Dragoman, M., Terahertz fields and Applications, Progress in Quantum Electronics, 28 (1), 1-66, 2004.

[33] Ryu, H. C., Kim, S. I., Kwak, M. H., Kang, K.Y., Park, S. O., A folded dipole antenna having extremely high input impedance for continuous-wave terahertz power enhancement, 33rd International Conference on Infrared, Millimeter, and Terahertz Waves, 15-19 September 2008 Pasadena, 1-2, 2008.

[34] Moon, K., Han, H., Park, I, Terahertz folded half-wavelength dipole antenna for high output power, International Topical Meeting on Microwave Photonics, IEEE, 12-14 October 2005 Seoul, 301-304, 2005.

[35] Baaske, K., Ezdi, K., Jördens, C., Peters, O., Mikulics, M., Koch, M., Folded dipole antenna for increased cw THz output power, 34th International Conference on Infrared, Millimeter, and Terahertz Waves, 21-25 September 2009 Busan, 1-2, 2009.

[36] Gitin, M. M., Wise, F. W., Arjavalingam, G., Pastol, Y., Compton, R. C., Broadband characterization of millimeter-wave log-periodic antennas by photoconductive sampling, IEEE Transactions on Antennas and Propagation, 42 (3), 335-339, 1994.

[37] Mendis, R., Sydlo, C., Sigmund, J., Feiginov, M., Meissner, P., Hartnagel, H. L., Tunable CW-THz system with a log-periodic photoconductive emitter, Solid-State Electronics. 48 (10-11), 2041-2045, 2004.

[38] Nguyen, T. K., Ho, T. A., Han, H., Park, I., Numerical study of self-complementary antenna characteristics on substrate lenses at terahertz frequency, Journal of Infrared, Millimeter, and Terahertz Waves, 33 (11), 1123-1137, 2012.

[39] McIntosh, K. A., Brown, E. R., Nichols K. B., McMahon, O. B., Terahertz photomixing with diode lasers in low-temperature-grown GaAs, Applied Physics Letters, 67 (26), 3844-3846, 1995.

[40] Sizov, F., Rogalski, A., THz detectors, Progress in Quantum Electronics, 34, 278-347, 2010.

[41] Duffy, S. M., Verghese, S., McIntosh., K. A., Jackson, A., Gossard, A. C., Matsuura, S., Accurate modeling of dual dipole and slot elements used with photomixers for coherent terahertz output power, IEEE Transactions on Microwave Theory and Techniques, 49 (6), 1032-1038, 2001.

[42] Verghese, S., McIntosh, K., Brown, E., Optical and terahertz power limits in the low-temperature-grown GaAs photomixers, Applied Physics Letters, 71 (19), 2743–2745, 1997.

[43] Mandviwala, T., Lail, B., Boreman, G., Infrared-frequency Coplanar striplines: design, fabrication, and measurements, Microwave and Optical Technology Letters, 47 (1), 17-20, 2005.

[44] Zhu, N., Ziolkowski, R. W., Photoconductive THz Antenna Designs With High Radiation Efficiency, High Directivity, and High Aperture Efficiency, IEEE Transactions on Terahertz Science and Technology, 3 (6), 721-730, 2013.

[45] Nguyen, T. K., Park, I., Effects of antenna design parameters on the characteristics of a terahertz coplanar stripline dipole antenna, Progress In Electromagnetics Research M, 28, 129-143, 2013.

[46] Han, K., Nguyen, T. K., Park, I., Han, H., Terahertz Yagi-Uda antenna for high input resistance, Journal of Infrared, Millimeter, and Terahertz Waves, 31 (4), 441-454, 2010.

[47] Nguyen, T. K., Han, H., Park, I., Full-wavelength dipole antenna on a hybrid GaAs membrane and Si lens for a terahertz photomixer, Journal of Infrared, Millimeter, and Terahertz Waves, 33 (3), 333-347, 2012.

[48] Woo, I, Nguyen, T. K., Han, H., Lim, H., Park, I., Four-leaf-clover-shaped antenna for a THz photomixer, Optics Express, 18 (18), 18532-18542, 2010.

[49] Nguyen, T. K., Kim, S., Rotermund F., Design of a wideband continuous-wave photomixer antenna for terahertz wireless communication systems, Journal of Electromagnetic Waves and Applications, 28 (8), 976-988, 2014.

[50] Nguyen, T. K., Han, H., Park, I., Numerical study of full-wavelength dipole antenna on a GaAs membrane structure at terahertz frequency, 32 (6), 763-777, 2011.

[51] Zienkiewicz, O. C., Taylor, R. L., Zhu, J. Z., The finite element method: Its basis and fundamentals, (6th ed.), Elsevier, Oxford, 2005.

[52] Sadiku, M. N. O., Numerical Techniques in Electromagnetics, CRC Press, United States: 2000.

[53] High Frequency Structure Simulator (HFSS), Ansoft Corporation, Pittsburgh, PA. Ver. 12.1, 2010.

[54] Gupta, K. C., Garg, R., Bahl, I., Bhartia, P., Microstrip lines and slotlines, (2nd ed.), Artech House, Boston, Massachusetts, 1996..

[55] Unlu, M., Topalli, K., Atasoy, H. I., Demir, S., Civi, O. A., Akin, T., Hybrid Connection of RF MEMS and SMT Components in an Impedance Tuner, AEU International Journal of Electronics and Communications, 64 (8), 748-756, 2010.

[56] Zohur, A., Mopidevi, H., Rodrigo, D., Unlu, M., Jofre, L., Cetiner, B. A., RF MEMS reconfigurable two-band antenna, IEEE Antennas and Wireless Propagation Letters, 12, 72-75, 2013.

[57] Unlu, M., Damgaci, Y., Mopidevi, H. S., Kaynar, O., Cetiner, B. A., Reconfigurable, tri-band RF MEMS PIFA antenna, International Antennas and Propagation Symposium, July 2011 Spokane, IEEE, 1563-1565, 2011.

[58] Balanis, C. A., Antenna theory: analysis and design, (3rd ed.), John Wiley & Sons Inc., New Jersey, 2005.

[59] Nguyen, C., Analysis Methods for RF, Microwave, and Millimeter-wave Planar Transmission Line Structures, John Wiley & Sons Inc., New Jersey, 2000.

[60] Antoniades, M. A., Eleftheriades, G. V., Multiband compact printed dipole antennas using NRI-TL metamaterial loading, IEEE Transactions on Antennas and Propagation, 60 (12), 5613-5626, 2012.

[61] Rumsey, V., Frequency independent antennas, 1958 IRE International Convention Record, 21-25 March 1966, 114-118, 1958.

[62] Baheti, A., Mehrabani A. M., Shafai L., Analysis of multi turn 4-arm Archimedean spiral antenna with varying spacing between arms, Progress in Electromagnetic Research Symposium, PIER, 27-30 March, 1554-1558, 2012.

[63] DuHamel, R. H., Logarithmically Periodic Antenna Designs, 1958 IRE Convention Record, 21-25 March 1966, 139-157, 1958.

[64] Pozar, D. M., Microwave Engineering, (3rd ed.), Wiley & Sons Inc., New Jersey, 2005